Progressive weakening within the overriding plate during dual inward dipping subduction

Zhibin Lei[1], J. H. Davies[1]

[1]School of Earth and Environmental Sciences, Cardiff University, Cardiff, CF10 3AT, UK

Correspondence to: Zhibin Lei (leiz2@cardiff.ac.uk)

Author Twitter handles: @Lei_geodynamics

Highlights:

1. Investigate dynamic internally driven dual inward dipping subduction models

2. Viscosity evolves as a function of multiple physical parameters

3. Self-consistently forms a fixed boundary condition and strong convective mantle flow

4. Strain rate weakening plays a dominant role in initiating viscosity reduction

Abstract

Dual inward dipping subduction often produces complex deformation patterns in the overriding plate. However, the geodynamic process of how dual inward dipping subduction relates to this deformation is still poorly understood. Here we apply a composite viscosity, dependent on multiple parameters, e.g., temperature, pressure, strain rate etc., in 2-D thermo-mechanical numerical modelling to investigate how dual inward dipping subduction modifies the rheological structure of the overriding plate. Three variables are investigated to understand what controls the maximum degree of weakening. We find that the initial length and thickness of the overriding plate are negatively correlated with the magnitude of viscosity reduction. While the initial thickness of the subducting plate positively relates to the magnitude of viscosity reduction. The progressive weakening can result in a variety of stretching states ranging from 1) little or no lithosphere thinning and extension, to 2) limited thermal lithosphere thinning, and 3) localised rifting followed by spreading extension. Compared with single sided subduction, dual inward dipping subduction further reduces the magnitude of viscosity of the overriding plate. It does this by creating a dynamic fixed boundary condition for the overriding plate and forming a stronger upwelling mantle flow underlying the overriding plate. Three types of feedback weakening cycles are recognised, among which the strain rate weakening mechanism plays the dominant role in lowering the viscosity of the overriding plate throughout the simulation. Strain rate weakening is also a precondition for initiating thermal weakening, strain localisation and lithosphere thinning.

Keywords: dual inward dipping subduction; composite viscosity; feedback weakening; numerical modelling.

1. Introduction

Subduction can pose a fundamental tectonic overprint on the overriding plate by generating a volcanic arc (Perfit et al., 1980; Straub et al., 2020), back-arc basin (Uyeda, 1981), orogeny (Faccenna et al., 2021), or even continental breakup (Dal Zilio et al., 2018). Most subduction zones involve only one subducting slab. Here we consider multiple subducting slabs, in particular dual inward dipping subduction. Dual inward dipping subduction, or bi-vergent subduction occurs when the overriding plate is decoupled with two subducting slabs dipping towards each other. It is one of the four most commonly described subduction zones with multiple slabs, i.e., inward-dipping, same-dip, outward-dipping and oppositely dipping adjacent subduction zones (Holt et al., 2017; Király et al., 2021).

Dual inward dipping subduction zones are often found in areas which exhibit complex geodynamic processes in their geological history. Seismic tomography shows that dual inward dipping subduction exists at the Caribbean plate between the Cocos slab and Lesser-Antilles subduction zone (Van Benthem et al., 2013), the Philippine islands between the Philippine trench and Manila trench (Wang and He, 2020), and South-East Asia between the Philippine and the Sumatra subduction (Hall and Spakman, 2015; Huang et al., 2015; Maruyama et al., 2007). In combination with seismic tomography, plate reconstructions have made it more evident that dual inward dipping subduction could have existed in some regions in the past (Faccenna et al., 2010; Hall and Spakman, 2015) constrained by suture zone petrology demonstrating oceanic floor closure. A good example is the North China Craton. Suture zone studies reveal that multiple inward dipping subduction may have surrounded the North China Craton from Early Paleozoic to Tertiary (Santosh, 2010; Windley et al., 2010). Despite these improved observations and evidence, dual inward dipping subduction is still poorly understood in terms of how it differs from single sided subduction in deforming or weakening the overriding plate.

Numerical investigations have been conducted to understand the dynamics of dual inward dipping subduction. Research shows that the initial slab dip of the subducting plate affects the upper mantle dynamic pressure between the convergent slabs and stress state within the overriding plate (Holt et al., 2017). Varying the distance between the trenches, convergence rate, and asymmetry of subducting plates can alter the topography of the overriding plate (Dasgupta and Mandal, 2018). The thickness of the plates and the lithosphere to asthenosphere viscosity ratio are all tested to investigate their effect on the slab geometry and the magnitude of mantle upwelling flow underlying the overriding plate (Lyu et al., 2019). These pioneering investigations show that dual inward dipping subduction can generate a variety of upper mantle flow patterns which regulate the stress state and topography of the overriding plate. However, these models all applied a simplified constant rheology for both plates and convective mantle flow, i.e., the viscosity is neither temperature, pressure nor stress-dependent. Mineral rheology experiments indicate that viscosity varies as a function of multiple parameters, e.g., temperature, pressure, stress, strain rate etc. (Bürgmann and Dresen, 2008; Burov, 2011; Hirth and Kohlstedt, 2003; Karato, 2010; Lynch and Morgan, 1987). Previous models with simplified rheology were unable to quantitatively calculate the softening effect due to slab rollback and/or induced mantle wedge flow. Also, the simplified rheology does not allow the lithosphere to weaken and produce new plate boundaries.

In this research, a series of 2-D thermo-mechanical and self-consistently driven models are run to investigate what role dual inward dipping subduction plays in altering the rheology within the overriding plate and identifying the underlying driving mechanism. The composite rheology law enables the viscosity to self-consistently evolve as a function of multiple varying variables including temperature, strain rate, stress and pressure.

2. Methods

We ran the thermally-driven dual inward dipping subduction models using the code Fluidity (Davies et al., 2011; Kramer et al., 2012), a finite-element control-volume computational modelling framework, with an adaptive mesh that is set up to capture evolving changes with a maximum resolution of 0.4 km in this research.

2.1 Governing equations and rheology setup

Under the Boussinesq approximation (McKenzie et al., 1974), the equations governing thermally driven subduction process are derived from conservation of mass, momentum, and energy, for an incompressible Stokes flow

$$\partial_i u_i = 0, \tag{1}$$

$$\partial_i \sigma_{ij} = -\Delta\rho g_j, \tag{2}$$

$$\frac{\partial T}{\partial t} + u_i \partial_i T = \kappa \partial_i^2 T, \tag{3}$$

in which u, g, σ, T, κ are the velocity, gravity, stress, temperature, and thermal diffusivity, respectively (Table 1). In particular, the full stress tensor σ_{ij} consists of deviatoric and lithostatic components via

$$\sigma_{ij} = \tau_{ij} - p\delta_{ij}, \tag{4}$$

where τ_{ij} represents the deviatoric stress tensor, p the dynamic pressure, and δ_{ij} the Kronecker delta function.

Table 1. Key parameters used in this research.

Quantity	Symbol	Units	Value
Gravity	g	$m\ s^{-2}$	9.8
Gas constant	R	$J\ K^{-1}\ mol^{-1}$	8.3145
Mantle geothermal gradient	G	$K\ km^{-1}$	0.5 (UM) 0.3 (LM)
Thermal expansivity coefficient	α	K^{-1}	3×10^{-5}
Thermal diffusivity	κ	$m^2\ s^{-1}$	10^{-6}
Reference density	ρ_s	$kg\ m^{-3}$	3300
Cold, surface temperature	T_s	K	273
Hot, mantle temperature	T_m	K	1573
Maximum viscosity	μ_{max}	$Pa \cdot s$	10^{25}
Minimum viscosity	μ_{min}	$Pa \cdot s$	10^{18}
Diffusion Creep			
Activation energy	*E*	$kJ\ mol^{-1}$	300 (UM) 200 (LM)
Activation volume	*V*	$cm^3\ mol^{-1}$	4 (UM) 1.5 (LM)
Prefactor	*A*	$Pa^{-n}\ s^{-1}$	3.0×10^{-11} (UM) 6.0×10^{-17} (LM)
	n		1
Dislocation Creep (UM)			
Activation energy	*E*	$kJ\ mol^{-1}$	540
Activation volume	*V*	$cm^3\ mol^{-1}$	12
Prefactor	*A*	$Pa^{-n}\ s^{-1}$	5.0×10^{-16}
	n		3.5
Peierls Creep (UM)			
Activation energy	*E*	$kJ\ mol^{-1}$	540
Activation volume	*V*	$cm^3\ mol^{-1}$	10
Prefactor	*A*	$Pa^{-n}\ s^{-1}$	10^{-150}
	n		20

Yield Strength Law			
Surface yield strength	τ_0	MPa	2
Friction coefficient	f_c		0.2
	$f_{c,weak}$		0.02 (weak layer)
Maximum yield strength	$\tau_{y,max}$	MPa	10,000

The deviatoric stress tensor and strain rate tensor $\dot{\varepsilon}_{ij}$ are related according to

$$\tau_{ij} = 2\mu\dot{\varepsilon}_{ij} = \mu(\partial_j u_i + \partial_i u_j), \tag{5}$$

with μ the viscosity. The density difference due to temperature is defined as

$$\Delta\rho = -\alpha\rho_s(T - T_s), \tag{6}$$

where α is the coefficient of thermal expansion, ρ_s is the reference density at the surface temperature T_s (Table 1).

The key rheology difference of the model setup with previous dual inward dipping subduction models (Dasgupta and Mandal, 2018; Holt et al., 2017; Lyu et al., 2019) is that the magnitude of viscosity throughout the model can self-consistently vary with time as the model evolves. The governing rheological laws are identical throughout the model domain, though the rheology parameters we use differ to match different deformation mechanisms observed at different depths in the Earth. In detail, a uniform composite viscosity is used to take account of four deformation mechanisms under different temperature-pressure conditions: diffusion creep, dislocation creep, Peierls mechanism, and yielding (Garel et al., 2014). The effective composite viscosity in the computational domain is given by

$$\mu = \left(\frac{1}{\mu_{diff}} + \frac{1}{\mu_{disl}} + \frac{1}{\mu_P} + \frac{1}{\mu_y}\right)^{-1}, \tag{7}$$

where μ_{diff}, μ_{disl}, μ_y define the creep viscosity following

$$\mu_{diff/disl/P} = A^{-\frac{1}{n}} exp\left(\frac{E + PV}{nRT_r}\right) \dot{\varepsilon}_{II}^{\frac{1-n}{n}}, \tag{8}$$

in which A is a prefactor, n the stress component, E the activation energy, P the lithostatic pressure, V the activation volume, R the gas constant, T_r the temperature obtained by adding an adiabatic gradient of 0.5 K/km in the upper mantle and 0.3 K/km in the lower mantle to the Boussinesq solution (Fowler, 2005), $\dot{\varepsilon}_{II}$ the second invariant of the strain rate tensor. Note that in the lower mantle only diffusion creep applies and the lower mantle is 30 times more viscous than the upper mantle. While the fourth deformation mechanism, yielding, is defined by a brittle-failure type yield-stress law as

$$\mu_y = \frac{\tau_y}{2\dot{\varepsilon}_{II}}, \tag{9}$$

with μ_y the yielding viscosity and τ_y the yield strength. τ_y is determined by

$$\tau_y = min(\tau_0 + f_c P, \tau_{y,max}), \tag{10}$$

with τ_0 the surface yield strength, f_c the friction coefficient, P the lithostatic pressure, and $\tau_{y,max}$ the maximum yield strength (Table 1).

2.2 Model setup

The computational domain is 10,000 km by 2,900 km, with x (width) coordinates and z (depth) coordinates extending from the surface to the bottom of the lower mantle (Figure 1). Such a wide domain reduces the influence of side and bottom boundary conditions (Chertova et al., 2012). The thermal boundary conditions at the surface and bottom are defined by two isothermal values: $T = T_s$ and $T = T_m$ for surface and base of lower mantle respectively, while the sidewalls are insulating. As for velocity boundary conditions, a free-surface is applied at the top boundary to enable trench mobility, while the other boundaries are free-slip.

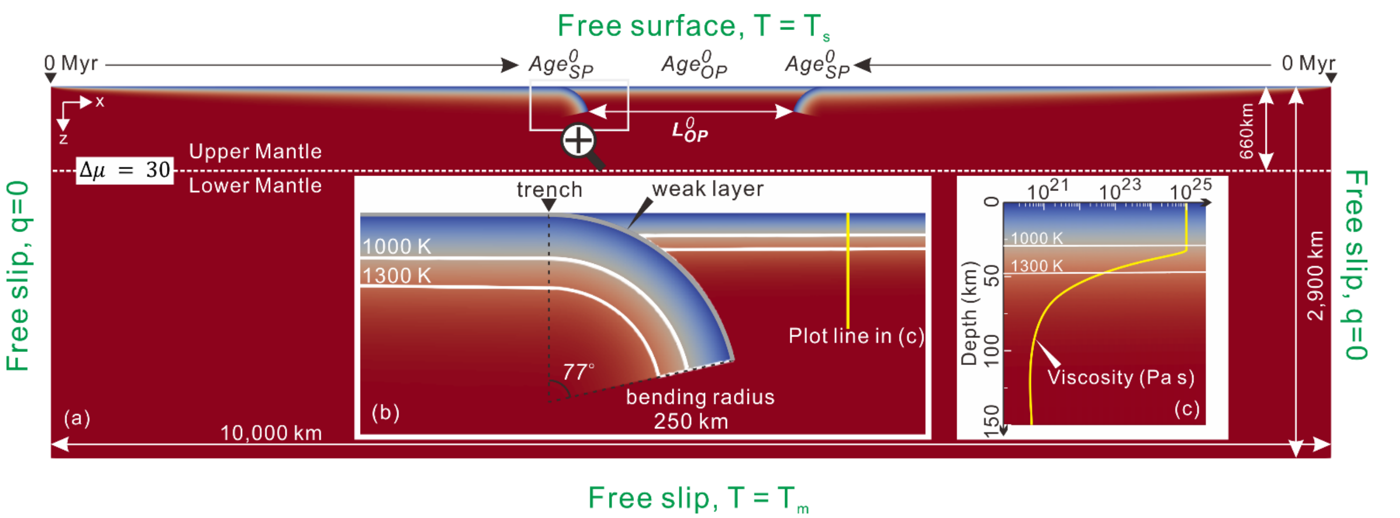

Figure 1. Dual inward dipping model geometry and initial setup illustrated with the initial temperature field as the background. (a) The whole computational domain. Age_{SP}^{0} and Age_{OP}^{0} represent the initial ages of subducting plate and overriding plate at trench. The viscosity jump ($\Delta\mu$) between upper and lower mantle at 660 km transition zone is set up with a fixed value of 30. To be noted, L_{OP}^{0} represents the distance between the leading tip edges of the slabs initially penetrating into the upper mantle. L_{OP}^{0} roughly equals the length of the overriding plate with constant thickness, excluding the overriding plate above the interface with the bending slab. (b) Enlarged area of the trench zone where the bending slab meets the flat overriding plate. The 1100 K and 1300 K isotherms are marked in white contours. (c) Vertical profile of viscosity against depth within the overriding plate. The plot line is 400 km away from the initial trench.

To simplify the complexity of the model, a laterally symmetric dual inward dipping subduction is applied, i.e., the model is strictly symmetric along the vertical middle line of the domain (5000 km away from the side boundaries) in all aspects, e.g., the geometry and rheology properties. Age_{SP}^{0} and Age_{OP}^{0} represent the initial ages of subducting plate and overriding plate at the trench, where the two plates meet at the surface. Laterally on the surface, the age of the subducting plates increases linearly with their distance away from the mid-ocean ridge on either side. While vertically, the age of the plate at surface defines the initial thermal structure through a half-space cooling model (Turcotte and Schubert, 2014),

$$T(x,z) = T_s + (T_m - T_s)erf\left(\frac{z}{2\sqrt{\kappa Age^0(x)}}\right), \tag{11}$$

with x the distance away from the mid-ocean ridge, *erf* the error function, z the depth, κ the thermal diffusivity. All parameters are listed in Table 1. The whole overriding plate is set up with a constant age. Thus, the thermal structure within the overriding plate is laterally homogeneous. The bottom of thermal lithosphere is defined as the isotherm of 1300 K, where the temperature gradient starts to drop quickly (Garel and Thoraval, 2021). The initial thickness of the subducting plate (H_{SP}^0) and overriding plate (H_{OP}^0) can be calculated using

$$H_{Plate}^0 = erfinv((T_{1300K} - T_s)/(T_m - T_s)) * 2 * \sqrt{\kappa * Age_{Plate}^0(x)}, \tag{12}$$

where H_{Plate}^0 is the initial thickness of the plate thermal lithosphere and *erfinv* is the inverse error function.

The free surface boundary condition together with the mid-ocean ridge setup allows the subducting slabs, and overriding plate and therefore the trench to move freely as subduction evolves. To initiate self-driven subduction without implementing external forces, the subducting plate is set up with a bend into the mantle and an 8 km thick low-viscosity decoupling layer on the top. This weak layer has the same rheology as the rest of the domain, other than its maximum viscosity is 10^{20} Pa s, and its friction coefficient is 0.02 (i.e. an order of magnitude lower). The initial bending radius is 250 km and the slab bends over 77 degrees from the trench (Figure 1).

2.3 Model variables

Three variables are investigated here: the initial length of the overriding plate (L_{OP}^{0}), the initial thickness of the subducting plate (H_{SP}^{0}) and overriding plate (H_{OP}^{0}) (Table 2). These are parameters also varied in previous research and therefore will allow easier comparison. H_{SP}^{0} and H_{OP}^{0} are dependent on plate age and calculated using Equation (12). The magnitude of L_{OP}^{0} that has been tested in previous models ranging from 500 km to 4000 km (Dasgupta and Mandal, 2018; Holt et al., 2017; Lyu et al., 2019), and the result shows that L_{OP}^{0} greater than 2500 km has little impact on the result (Lyu et al., 2019). Here L_{OP}^{0} is tested in the range from 500 km to 1600 km. The values of H_{SP}^{0} and H_{OP}^{0} that has been tested before ranges from 75-125 km and 75-150 km separately and those models suggest that H_{SP}^{0} is more important in deciding the magnitude of upwelling mantle flow than H_{OP}^{0} (Lyu et al., 2019). So the range of H_{SP}^{0} is extended to 94-141 km while the range of H_{OP}^{0} is narrowed down to 67-100 km.

Table 2. List of model setup.

Model name	L_{OP}^{0} (km)	H_{SP}^{0} (km)	H_{OP}^{0} (km)	Age_{SP}^{0} (Ma)	Age_{OP}^{0} (Ma)
$H_{SP}^{0} = 94\ km$	500	94	67	90	45
$H_{SP}^{0} = 100\ km$	500	100	67	100	45
$H_{SP}^{0} = 111\ km$	500	111	67	125	45
$H_{SP}^{0} = 122\ km$	500	122	67	150	45
$H_{SP}^{0} = 141\ km$	500	141	67	200	45
$H_{OP}^{0} = 67\ km$	500	141	67	200	45
$H_{OP}^{0} = 70\ km$	500	141	70	200	50
$H_{OP}^{0} = 74\ km$	500	141	74	200	55
$H_{OP}^{0} = 77\ km$	500	141	77	200	60
$H_{OP}^{0} = 100\ km$	500	141	100	200	100
$L_{OP}^{0} = 500\ km$	500	141	67	200	45

$L_{OP}^{0} = 600\ km$	600	141	67	200	45
$L_{OP}^{0} = 700\ km$	700	141	67	200	45
$L_{OP}^{0} = 800\ km$	800	141	67	200	45
$L_{OP}^{0} = 1000\ km$	1000	141	67	200	45
$L_{OP}^{0} = 1200\ km$	1200	141	67	200	45
$L_{OP}^{0} = 1600\ km$	1600	141	67	200	45

Models are named with the variable tested, e.g., $H_{SP}^{0} = 94\ km$ and $H_{SP}^{0} = 122\ km$ corresponds to the initial subducting plate thickness of 94 km and 122 km separately, while the initial overriding plate length and thickness in both models remain the same as 500 km and 67 km.

3. Results

3.1 Varying viscosity in an evolving model: an example

The thermal-mechanical model setup of this research enables self-consistent subduction. Similar to the self-consistent single subduction numerical and analogue models, subduction starts with a non-steady state phase where negative buoyancy pulls the slab to sink into the deeper mantle (e.g., Capitanio et al., 2010; Gerya et al., 2008; Schellart and Moresi, 2013). Following this short period of adjustment, the slab interacts with the lower mantle and steady state subduction ensues. We next describe in detail the dynamic evolution of dual inward dipping subduction for the model '$L_{OP}^{0} = 1200\ km$'.

3.1.1 Non-steady state subduction

During the non-steady state subduction, symmetric subduction develops about the midline of the overriding plate (~5000km away from the side boundaries). As more slab is pulled into the mantle, the negative buoyancy grows gradually. It takes ~5.8 Myr before the slab starts to interact with the lower mantle (Figure 2).

Convective mantle wedge flow is generated as the subducting slab bends and sinks in the upper mantle. The size of the convective cell grows with time and forms a crescent shape as wide as ~500 km before the slab reaches the depth of lower mantle. The convective cell is composed of a narrow downwelling flow coupling close to the sinking slab and a wide upwelling flow further away. The upwelling flow fades gradually as its distance away from the subducting slab increases. In the model '$L_{OP}^{0} = 1200\ km$', the two sets of wedge flow have little interaction and can be considered as two separate units. This is because the length of the overriding plate is 1200 km, which is greater than two times the width (~500 km) of a convection cell.

The overriding plate exhibits a widespread extensional stress field as a result of continuous subduction and the induced convective mantle wedge flows. Only a limited area close to the interface with the bending slabs develops compression (Figure 2, a). The widespread extensional stress field implies that the overriding plate has an overall stretching tendency. Within the overriding plate, the governing deformation mechanism is spatially layered (Figure 2, b). At depths shallower than 30 km within the overriding plate, yielding (brittle or plastic) deformation dominates. Underlying the yielding layer lies ~10 km thick Peierls creep layer. While for depths from ~40 km to the bottom of the thermal lithosphere deformation is dominated by dislocation creep. High strain rate areas are observed within and underneath the overriding plate (Figure 2, c). The thermal thickness of the overriding plate, defined by the 1300 K isotherm contour, does not change much throughout the simulation.

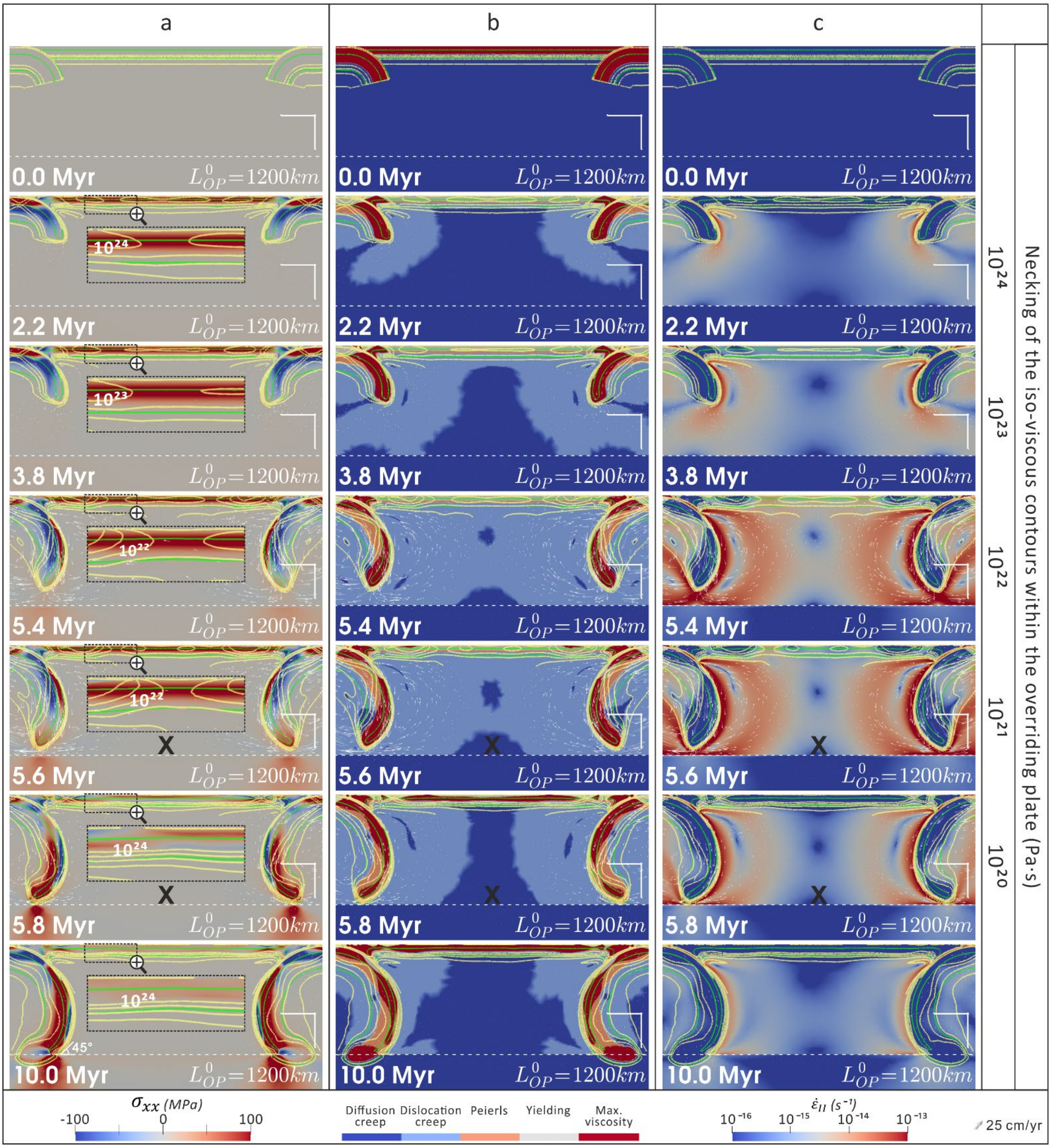

Figure 2. The Simulation screenshots of model '$L_{OP}^{0} = 1200\ km$'. (a) Horizontal stress component where positive value represents stretching and negative value denotes compression. (b) The dominant deformation mechanism. (c) Magnitude of second invariant of strain rate. The progressive weakening process within the overriding plate is demonstrated by the necking of the iso-viscous contours. The 5 groups of yellow contours encompassing the plates in each screenshot are iso-viscous contours of $10^{24}, 10^{23}, 10^{22}, 10^{21}, 10^{20}\ Pa \cdot s$ from outward to inward. Screenshot with a bold 'X' underlying the overriding plate means there is no necking developing in that timestep for the iso-viscous contour whose value is noted on the right-hand side, e.g., $10^{21}\ Pa \cdot s$. The two sets of green solid lines are 700 K and 1300 K isotherm contours to image the geometry of the plate. The transition zone at the depth of 660 km is marked by the horizontal white dashed line. The white right-angle scale bar lying above the right end of the transition zone represents 200 km in both directions. The bottom left corner caption shows the elapsed simulation time and bottom right corner is the name of the model.

The non-Newtonian rheology laws applied define viscosity as a function of multiple variables, e.g., temperature, pressure, stress, strain rate etc. As subduction initiates, it creates rheology heterogeneities within what initially was a laterally homogeneous overriding plate, allowing part of it to become weaker than other parts. To visualize the variation in lithosphere viscosity, several levels of iso-viscous contours are plotted, e.g., $10^{24}, 10^{23}, 10^{22}, 10^{21}\ Pa \cdot s$ (Figure 2). Here, the overriding plate weakening level is defined as the maximum order of viscosity magnitude drop. That is, weakening level 'I', 'II', 'III', 'IV' represents that the iso-viscous contour $10^{24}, 10^{23}, 10^{22}, 10^{21} Pa \cdot s$ is necked within the overriding plate respectively. It shows that the homogeneous overriding plate is gradually segmented into three strong cores connected with two low viscosity necking regions. Strain deformation is likely to localize upon these two necking areas and continuously lower the magnitude of viscosity therein. The minimum viscosity achieved in the overriding plate for model '$L_{OP}^{0} = 1200\ km$' is $10^{21} \sim 10^{22}\ Pa \cdot s$ (weakening level 'III'). The distance between these two necking regions is ~620 km (Figure 2, a, 3.8Myr). These necking regions match well with the high strain rate areas developed in the overriding plate. The initial result suggests that high strain rate may play an important role in softening the overriding plate during dual inward dipping subduction.

3.1.2 Steady state subduction

The steady state subduction process initiates after a short period of transition once slabs start to interact with the lower mantle. Due to the viscosity increase as the sinking slab enters the lower mantle at 660 km depth, it slows down, and the induced mantle wedge flow gets much weaker. After this, the model enters a steady state subduction process where mobility becomes slow and constant, and deformation reduces. Meanwhile, the necking of the iso-viscous contours is reversed by a cooling and healing process within the overriding plate (Figure 2). At the end of the 10 Myr simulation, the dip between the top of bending slab and the transition zone is ~45° and the total trench retreat is ~100 km.

3.2 Length of the overriding plate

The first series of models investigate decreasing the initial length of the overriding plate (L_{OP}^{0}) from 1600 km to 500 km, while keeping the initial thickness of the subducting and overriding plate as 141 km and 67 km separately. As L_{OP}^{0} decreases, the two symmetric subducting slabs become closer. The two separate convective mantle wedge flows start to combine with each other and form a stronger joint upwelling flow underneath the overriding plate (Figure 3). Consequently, as L_{OP}^{0} is reduced, the two separate necking areas within the overriding plate get closer and merge into a single one in the end. Also as L_{OP}^{0} is reduced it takes less time to lower each level of viscosity within the overriding plate during the non-steady state subduction. Besides, the progressive weakening process can go further and neck the $10^{21}\ Pa\ s$ iso-viscous contour (weakening level 'IV') when L_{OP}^{0} reaches <= 800 km, initiating significant lithosphere thinning and even rifting or spreading extension within the overriding plate (Figure 3, b-c). The significant extension usually lasts less than 1 Myr before it gradually stops after the slab reaches the depth of the lower mantle, but it causes substantial changes to the dual inward dipping subduction system. For example, significant slab rollback starts to develop, creating a flattening slab geometry in the upper mantle and steepening dip angle (45° to 75°, Figure 3) at the transition zone depth by the end of the 10 Myr simulation.

It is noted that the continuous thinning of the thermal lithosphere only initiates when the iso-viscous contour of $10^{21}\,Pa\cdot s$ starts to neck. This implies a potential coupling of the thermal lithosphere and the rheology boundary layer (usually defined as the depth of $10^{21}\,Pa\cdot s$) in the model. All models necking $10^{21}\,Pa\cdot s$ will continue to neck lower magnitudes of viscosity, e.g., $10^{20}, 10^{19}\,Pa\cdot s$. Simultaneously, the upwelling hot mantle flow can then ascend to fill the thinning region and create a new plate boundary (rifting extension) or even new sea floor (spreading extension) after it ascends to the surface. Thus, the ability to neck $10^{21}\,Pa\cdot s$ (or not) can be used as a key diagnostic to predict whether a new spreading ridge (new plate boundary) develops within the overriding plate (or just limited thinning).

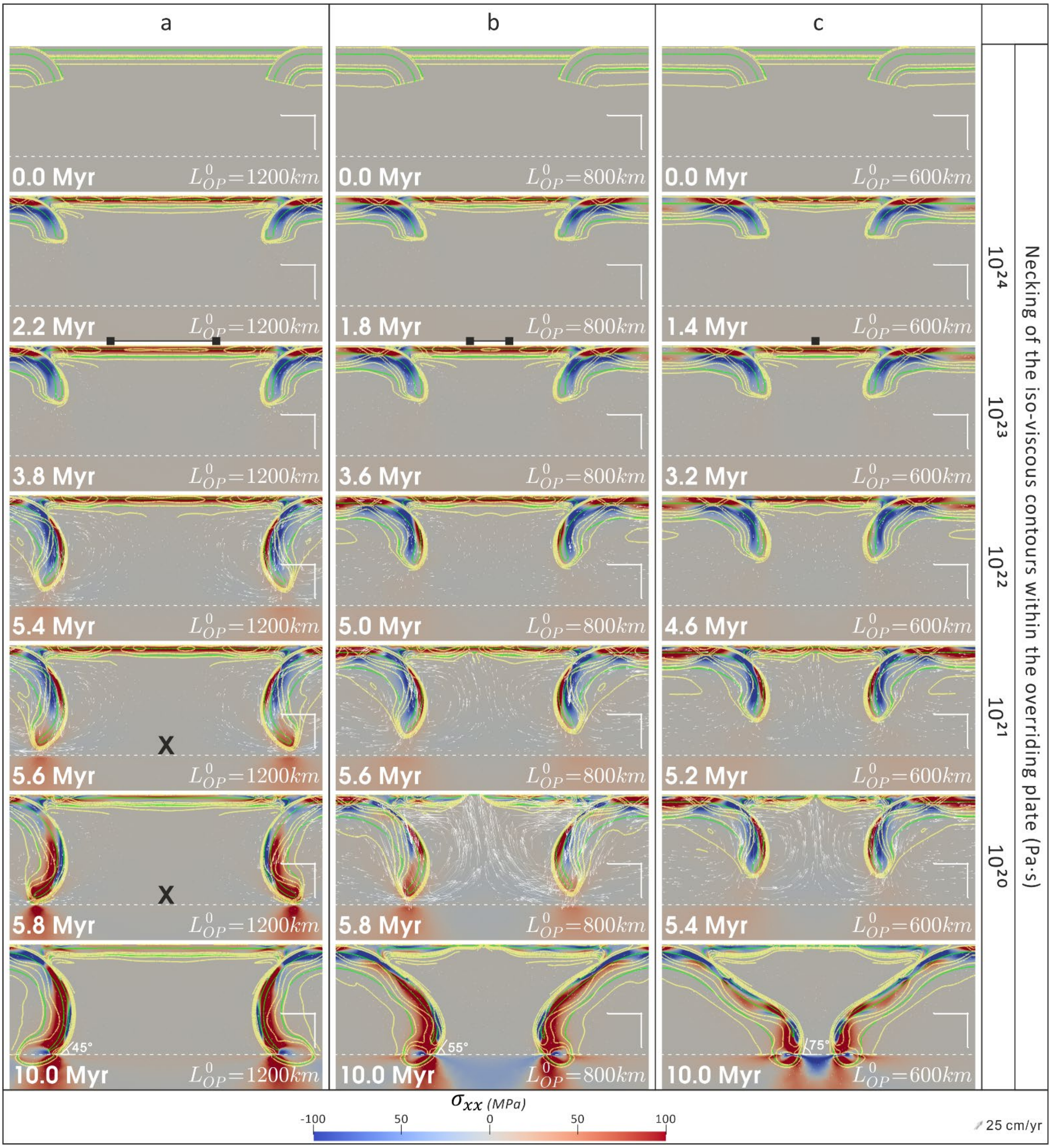

Figure 3. Progressive weakening of the overriding plate during dual inward dipping subduction with decreasing length of the overriding plate, (a) model '$L^0_{OP} = 1200\ km$', (b) model '$L^0_{OP} = 800\ km$', (c) model '$L^0_{OP} = 600\ km$'. The location of necked regions in the overriding plate are marked with black squares. A detailed explanation of the contours and symbols could be found in the caption of Figure 2.

To take a closer look at the extension behaviour within the overriding plate, we plot the evolving magnitude of viscosity at 5km depth (Figure 4). The filled region in the figure represents the overriding plate, therefore its widening represents extension within the overriding plate. As the initial length of the overriding plate (L_{OP}^{0}) decreases from 1600 km to 500 km, the total extension in the 10 Myr simulations increases from ~100 km (Figure 4, a-c) to 400~600 km (Figure 4, d-g). In detail, it is noted that extensional behaviour only become observable after the iso-viscous contour of $10^{23}\ Pa \cdot s$ is necked, i.e., after weakening level 'II' is achieved. Extension combining with lithospheric thinning only becomes significant when the iso-viscous contour $10^{21}\ Pa \cdot s$ is necked, i.e., when weakening level 'IV' is achieved. The highest weakening level achieved within the overriding plate increases from 'II' ($L_{OP}^{0} = 1600\ km$) to 'III' ($L_{OP}^{0} = 1000\ km$) and on to 'IV' ($L_{OP}^{0} \leq 800\ km$). During the spreading extension period, a highly centralised spreading centre (Figure 4, d,f-g) is observed in the middle of the overriding plate (Figure 4, d,f-g), while multiple spreading centres are observed to accommodate the extension in model '$L_{OP}^{0} = 700\ km$' (Figure 4, e).

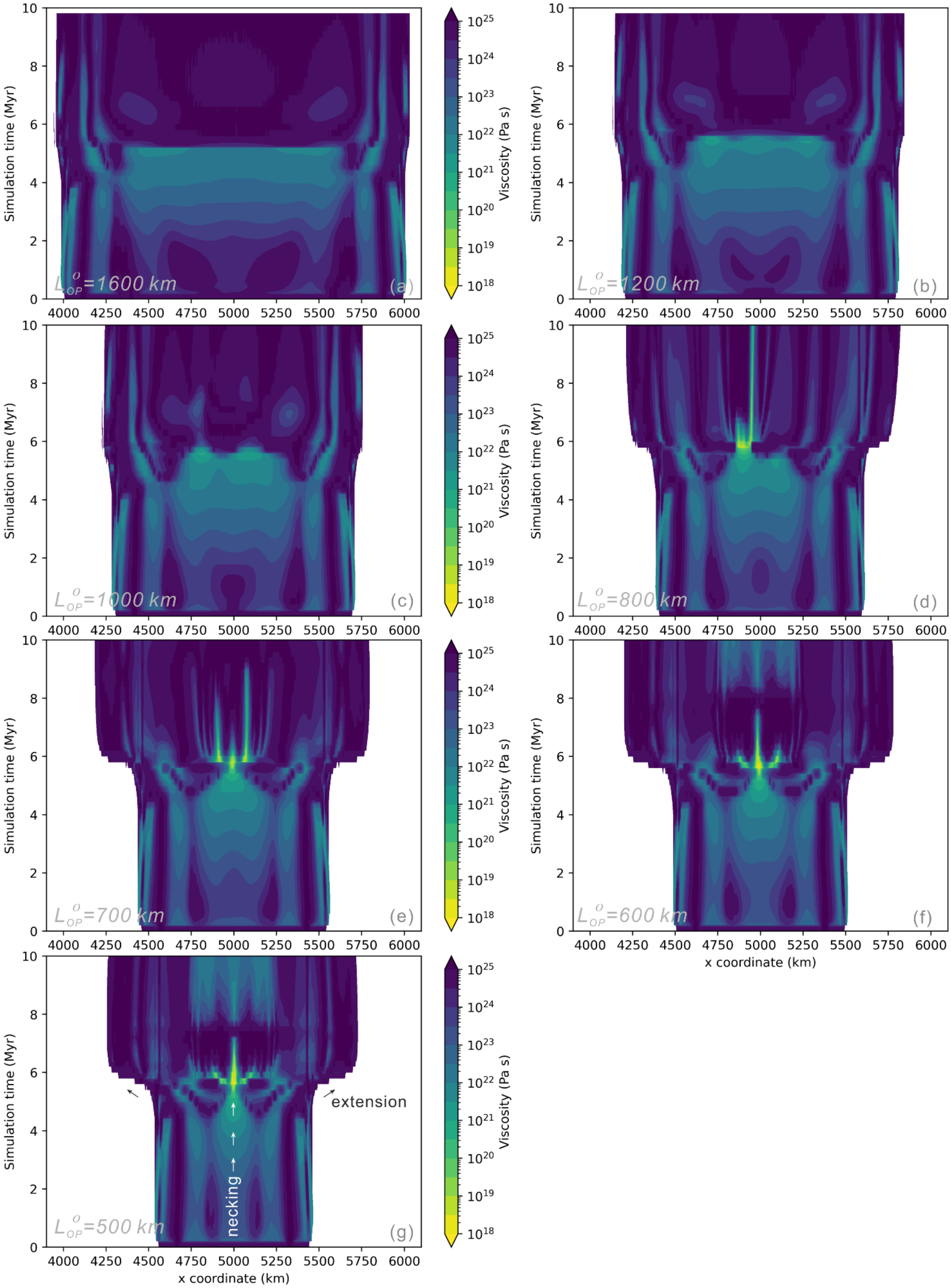

Figure 4. Temporal evolution of viscosity magnitude along the depth of 5 km within the overriding plate for models with different length of the overriding plate. (a) Model '$L^0_{OP} = 1600\ km$'. (b) Model '$L^0_{OP} = 1200\ km$'. (c) Model '$L^0_{OP} = 1000\ km$'. (d) Model '$L^0_{OP} = 800\ km$'. (e) Model '$L^0_{OP} = 700\ km$'. (f) Model '$L^0_{OP} = 600\ km$'. (g) Model '$L^0_{OP} = 500\ km$'. All models have the same setup of H^0_{SP} (141 km) and H^0_{OP} (67 km). The edge of the filled contour in the lateral direction represents the interface between the overriding plate and subducting plate. The white arrows display the necking process of the overriding plate.

Apart from the necking regions that may develop into rifting extension within the overriding plate, there are some secondary necking regions developed close to the trench (Figure 4). The maximum weakening level is 'II' in these secondary necking regions and the viscosity reduction stops after ~4 Myr into the simulation. The lateral distance away from the nearest trench of these secondary necking regions are equal, showing little correlation with the varying L_{OP}^{0}.

3.3 Thickness of the overriding plate

The second series of models increase the initial thermal thickness (defined by the 1300 K contour) of the overriding plate (H_{OP}^{0}) from 67 km to 100 km (Figure 5), while keeping the subducting plate's thickness (H_{SP}^{0}) and the length of the overriding plate (L_{OP}^{0}) constant (Table 2). As H_{OP}^{0} increases, the maximum weakening level developed within the overriding plate drops from 'IV' ($H_{OP}^{0} = 67\ km$) to 'III' ($H_{OP}^{0} = 74\ km$) and less than 'I' ($H_{OP}^{0} = 100\ km$). The time it takes to lower each order of viscosity magnitude increases, indicating a slower progressive weakening.

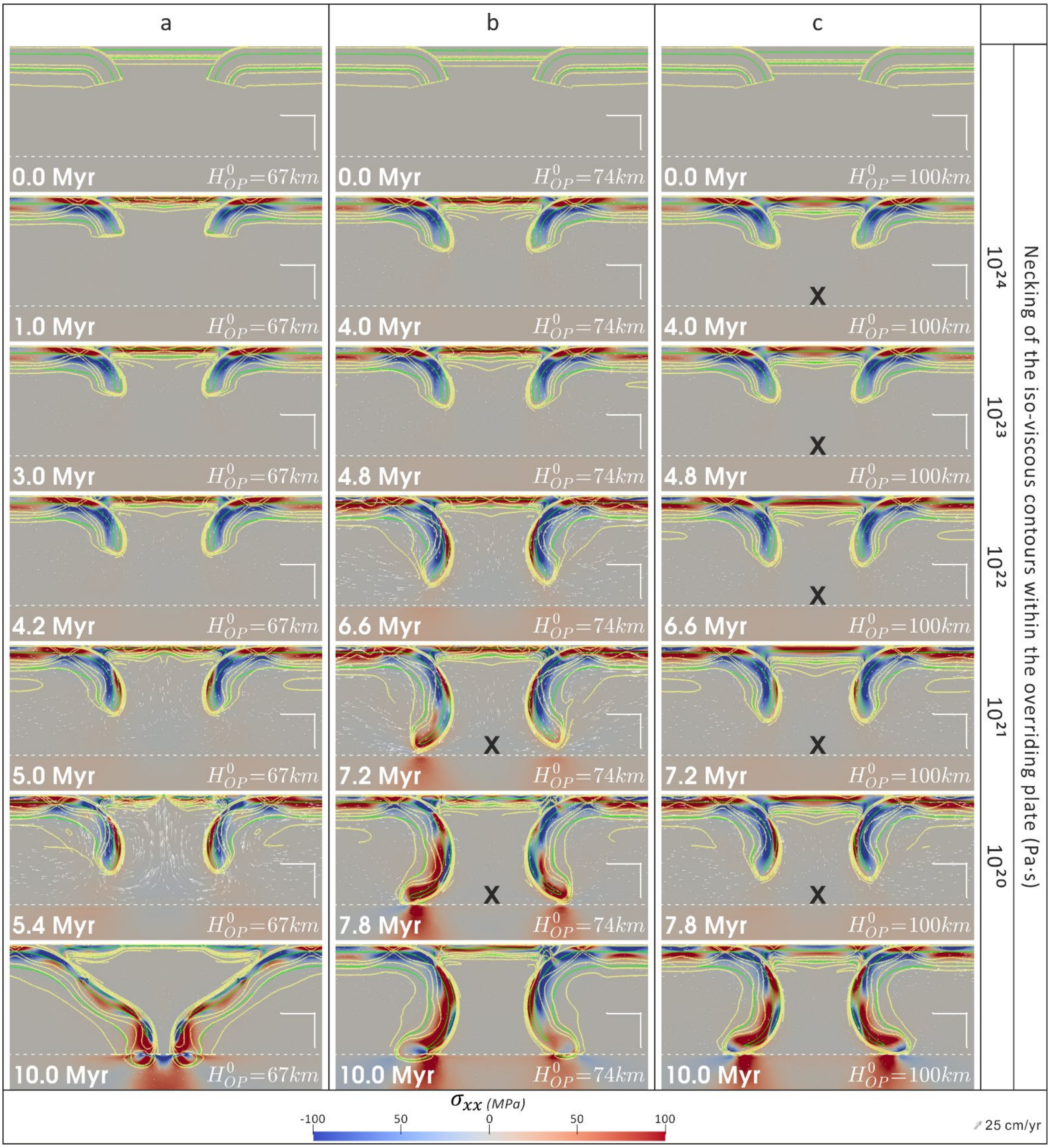

Figure 5. Progressive weakening, illustrated by visualising the stress σ_{xx}, of the overriding plate during dual inward dipping subduction with increasing thickness of the overriding plate, (a) model '$H^0_{OP} = 67\ km$', (b) model '$H^0_{OP} = 74\ km$' and (c) model '$H^0_{OP} = 100\ km$'. A detailed explanation of the contours and symbols could be found in the caption of Figure 2.

Besides, the total extension decreases from ~600 km ($H^0_{OP} = 67\ km$, Figure 6, a) to ~350 km ($H^0_{OP} = 70\ km$, Figure 6, b) and ultimately to ~0 km ($H^0_{OP} = 100\ km$, Figure 6, c-e). The maximum viscosity reduction in both the primary and secondary necking regions decreases as H^0_{OP} increases, while the lateral distance away from the trench of necking regions are equal, showing no correlation with H_{OP}^{0}.

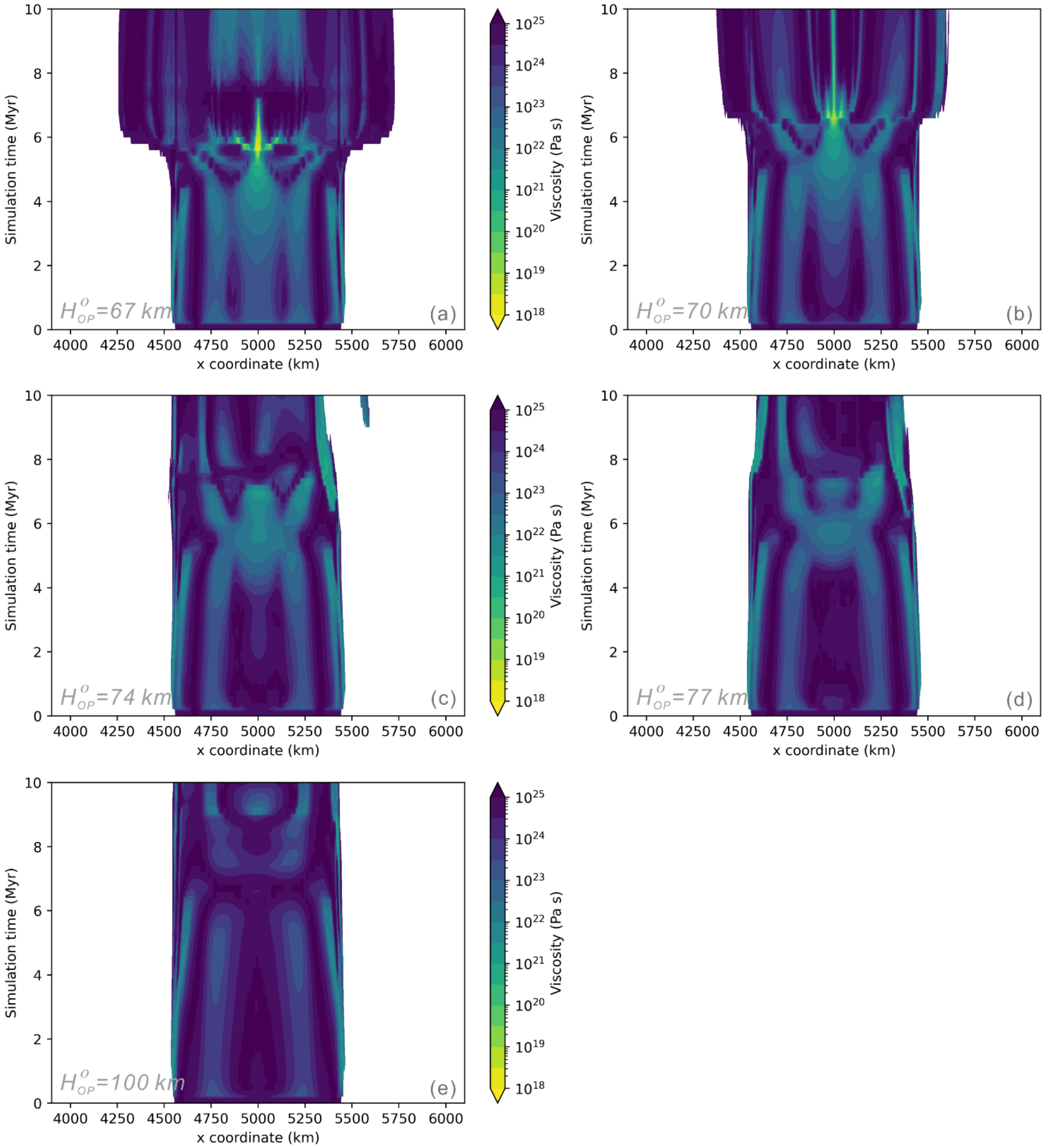

Figure 6. Temporal evolution of viscosity along a horizontal line at the depth of 5km in the overriding plate. (a) Model '$H_{OP}^{0} = 67\ km$'. (b) Model '$H_{OP}^{0} = 70\ km$'. (c) Model '$H_{OP}^{0} = 74\ km$'. (d) Model '$H_{OP}^{0} = 77\ km$'. (e) Model '$H_{OP}^{0} = 100\ km$'. All models have the same H_{SP}^{0} (141 km) and L_{OP}^{0} (500 km). The edge of the contour filling in the lateral direction represents the interface between the overriding plate and subducting plate.

To investigate the details of the progressive weakening in the necking region, 6 diagnostics are evaluated along the vertical slice in the middle of the overriding plate. This is where the necking belt develops in models with L_{OP}^{0} of 500 km. The diagnostics are integrated along the vertical slice and then divided by the thickness of the plate (Equation (13)),

$$\overline{D} = \frac{1}{H_{OP}} \int_{0}^{H_{OP}} D \; dy, \tag{13}$$

in which D represent the diagnostic. The averaged results include magnitude of viscosity ($\bar{\mu}$), second invariant of strain rate ($\overline{\dot{\varepsilon}_{II}}$), lithosphere thickness ($\overline{d_{OP}}$), horizontal stretching stress component ($\overline{\sigma_{xx}}$), vertical velocity component ($\overline{v_y}$), and temperature ($\bar{T}$).

Take the model '$H_{OP}^{0} = 67\ km$' for example (blue line), the evolution of the 6 diagnostics during dual inward dipping subduction is analysed (Figure 7). There is linear increase of $\overline{\dot{\varepsilon}_{II}}$ and $\overline{\sigma_{xx}}$, and linear decrease of $\bar{\mu}$ during the simulation between 1 Myr to 4 Myr. While $\overline{d_{OP}}$, $\bar{T}$ and $\overline{v_y}$ remains nearly constant. From 4 Myr to 5 Myr, $\overline{\dot{\varepsilon}_{II}}$ and $\bar{\mu}$ keep a similar linear trend as before. But $\overline{\sigma_{xx}}$ stops increasing and starts to decrease gently. $\overline{v_y}$ starts to increase and $\overline{d_{OP}}$ starts to decrease, while $\bar{T}$ experiences little change. During the rifting and spreading extension between 5 Myr to 6 Myr, all diagnostics are varying more rapidly, with $\bar{\mu}$, $\overline{d_{OP}}$ and $\overline{\sigma_{xx}}$ dropping and $\overline{\dot{\varepsilon}_{II}}$, $\overline{v_y}$ and $\bar{T}$ climbing steeply. Afterwards, the model enters the steady state subduction stage, and the weakening process is replaced by a healing process where $\bar{\mu}$ and $\overline{d_{OP}}$ both increase while $\overline{\dot{\varepsilon}_{II}}$ and $\overline{v_y}$ decrease gradually.

As the thickness of the overriding plate increases from 67 km to 100 km, the magnitude of viscosity drop in the necking area decreases. In detail, the plotting shows that if $\bar{\mu}$ in the necking area of the overriding plate is above $\sim 2 \times 10^{22}\ Pa \cdot s$ (Figure 7, a, grey dashed line), there is no lithospheric thinning in the necking region (Figure 7, c, purple and red lines). In the timesteps when $\bar{\mu}$ is in the range of $10^{21} \sim 2 \times 10^{22}\ Pa \cdot s$, thinning starts to build up, but it's not weak enough to have rifting extension (Figure 7, c, green line). Only when the $\bar{\mu}$ drops below $10^{21}\ Pa \cdot s$ does significant thinning develop within the overriding plate (Figure 7, c, blue and orange lines). The results of $\bar{\mu}$ confirms that the iso-viscous contour $10^{21}\ Pa \cdot s$ can be used to predict if rifting or spreading extension develops during the dual inward dipping subduction. It also reveals a more precise maximum viscosity below which the thinning of lithosphere develops.

The average temperature ($\bar{T}$) of the thermal lithosphere is ~850 K for all models. In models where iso-viscous contour of $10^{21}\ Pa \cdot s$ is necked, there are some thermal fluctuations as high as ~150 K. In detail, the transient heating up only takes place during the rifting extension process of the overriding plate, and $\bar{T}$ returns to ~850 K gradually during the spreading extension when new oceanic floor cools down quickly.

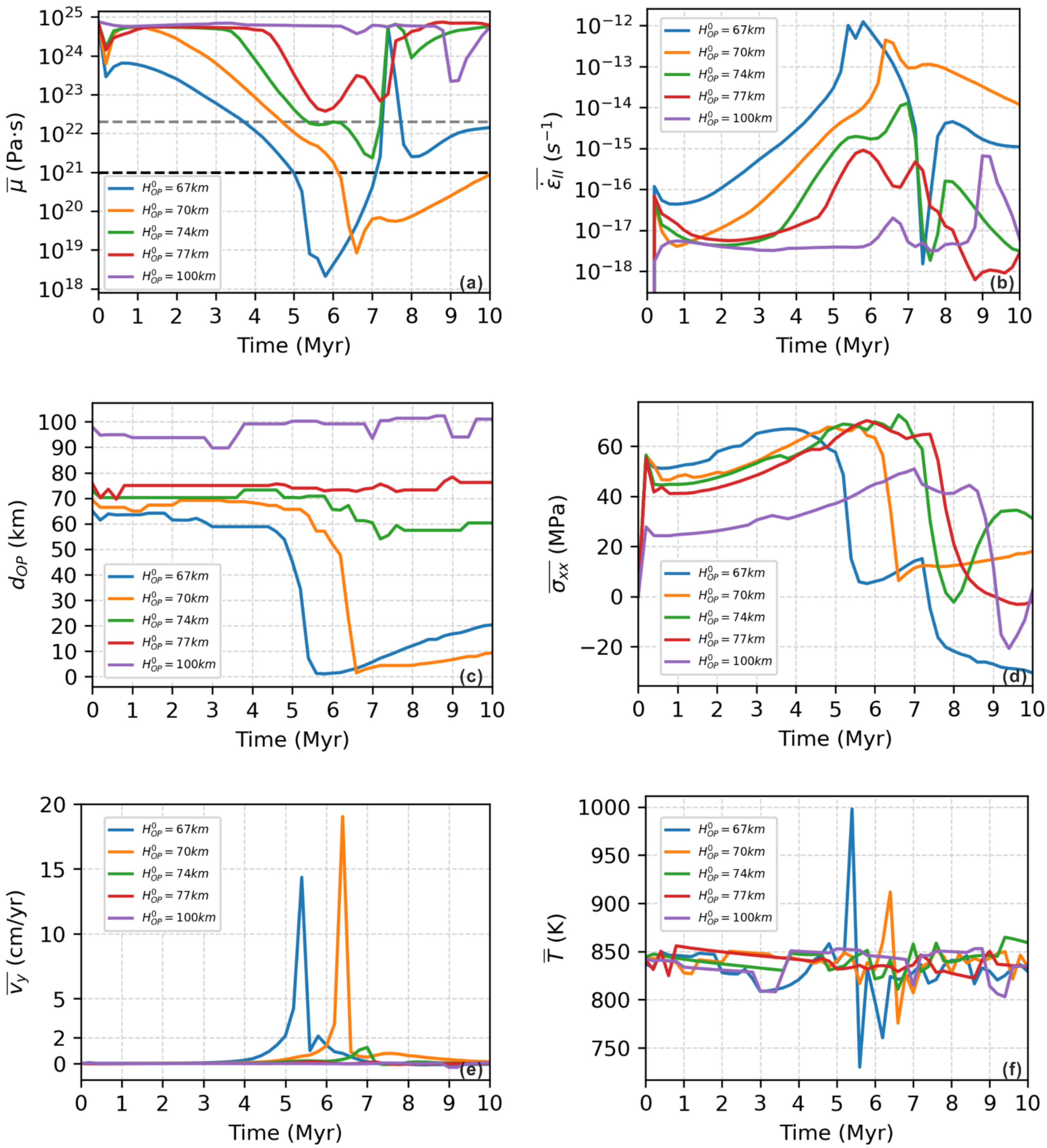

Figure 7. Temporal evolution of averaged diagnostics along the vertical slice in the middle of the overriding plate, (a) viscosity ($\bar{\mu}$), (b) second invariant of strain rate ($\overline{\dot{\varepsilon}_{II}}$), (c) lithosphere thickness ($\overline{d_{OP}}$), (d) horizontal stretching stress component ($\overline{\sigma_{xx}}$), (e) vertical velocity component ($\overline{v_y}$), and (f) temperature ($\bar{T}$). Positive value of $\overline{v_y}$ represent upward motion. We note the noisier $\bar{T}$ is a result of temperature also controlling the thickness of integration.

3.4 Thickness of the subducting plate

The third series of models investigate increasing the initial thermal thickness (again as defined by the 1300 K contour) of the subducting plate (H_{SP}^0) from 94 km to 141 km (Figure 8), while keeping the subducting plate's thickness (H_{OP}^0) and the length of the overriding plate (L_{OP}^0) constant. As H_{SP}^0 increases, the maximum weakening level developed within the overriding plate drops from 'I' ($H_{SP}^0 = 94\ km$) to 'III' ($H_{SP}^0 = 122\ km$) and 'IV' ($H_{SP}^0 = 141\ km$). The time it takes to lower each order of viscosity magnitude decreases, indicating a faster progressive weakening.

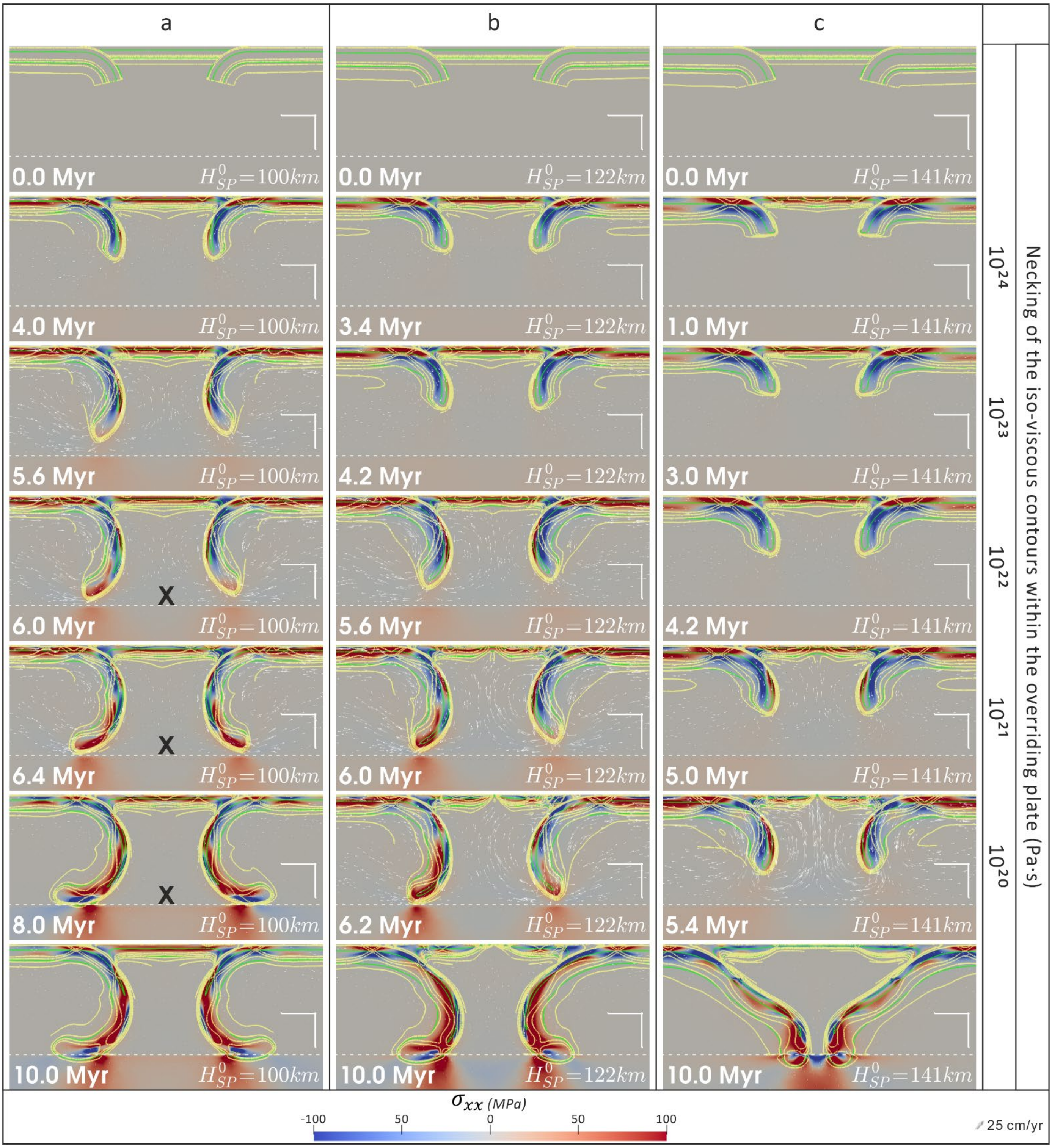

Figure 8. Progressive weakening of the overriding plate during dual inward dipping subduction with increasing age of the subducting plate. (a) Model '$H_{SP}^0 = 100\ km$'. (b) Model '$H_{SP}^0 = 122\ km$'. (c) Model '$H_{SP}^0 = 141\ km$'. A detailed explanation of the contours and symbols could be found in the caption of Figure 2.

Besides, the total extension increases from ~0 km ($H_{SP}^0 \leq 111\ km$, Figure 9, a-c) to ~200 km ($H_{SP}^0 = 122\ km$, Figure 9, d) and ultimately to ~600 km ($H_{SP}^0 = 141\ km$, Figure 9, e). The maximum viscosity reduction in both the primary and secondary necking regions increases as H_{SP}^0 increases, while the lateral distance away from the trench of necking regions are equal, showing little correlation with H_{SP}^{0}.

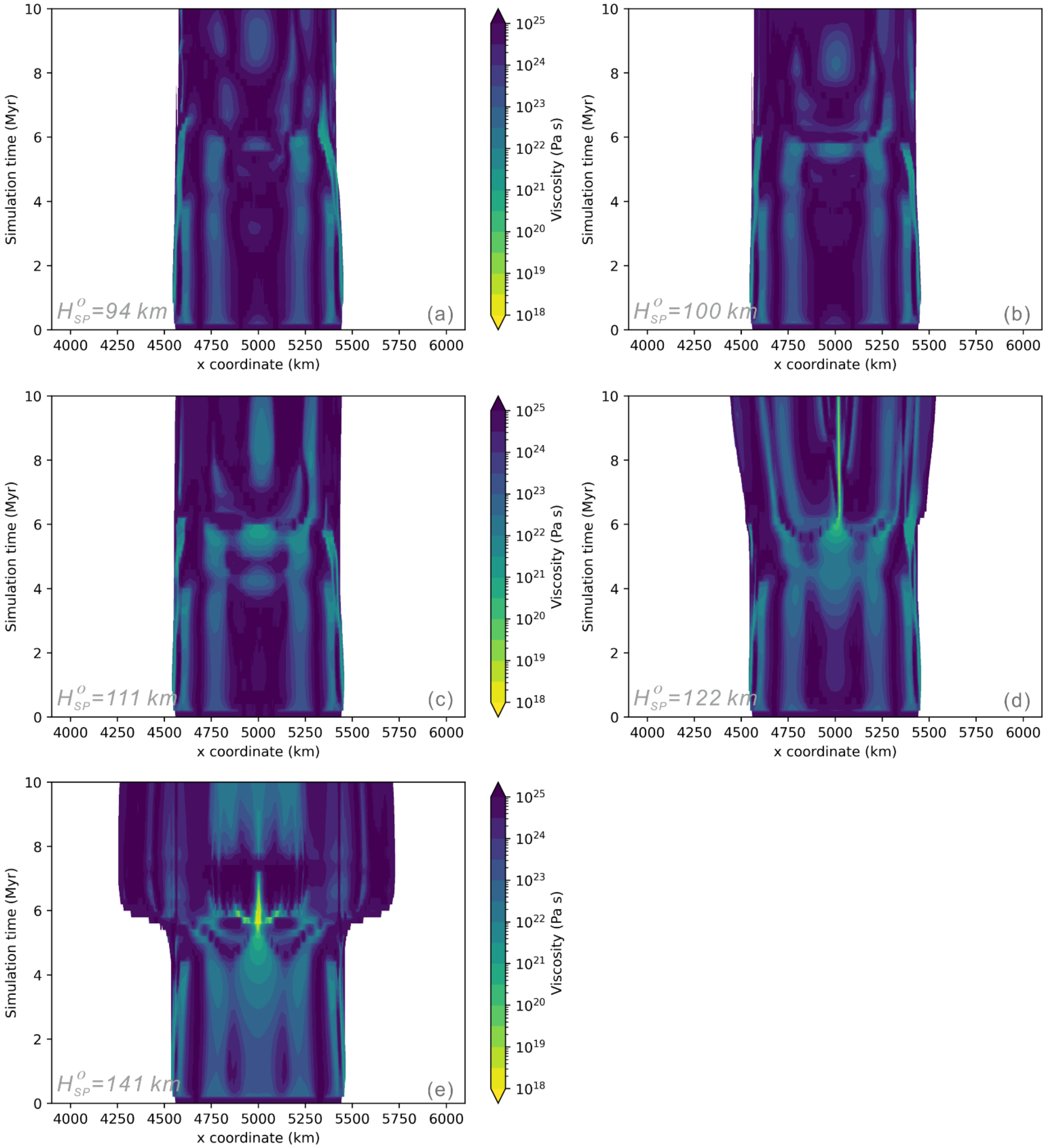

Figure 9. Temporal evolution of viscosity along a horizontal line at the depth of 5km in the overriding plate. (a) Model '$H_{SP}^{0} = 94\ km$'. (b) Model '$H_{SP}^{0} = 100\ km$'. (c) Model '$H_{SP}^{0} = 111\ km$'. (d) Model '$H_{SP}^{0} = 122\ km$'. (e) Model '$H_{SP}^{0} = 141\ km$'. Both models have the same H_{OP}^{0} (67 km) and L_{OP}^{0} (500 km). The edge of the contour filling in the lateral direction represents the interface between the overriding plate and subducting plate.

3.5 Regime of stretching state

A variety of deformation patterns and stretching state within the overriding plate have been observed when varying L_{OP}^0, H_{OP}^0 and H_{SP}^0. Several diagnostics are reported together to quantify the deformation developed within the overriding plate during the 10 Myr simulation (Table 3). The detail of each diagnostic is described as follows.

Table 3. Summary of diagnostics for all models. For further description of the diagnostics please see the main text.

Model name	weakening level	t_{rift} (Myr)	t_{660} (Myr)	$\bar{v}_{sink}$ (cm/yr)	l_{n2n} (km)	l_{n2t} (km)	total strain
$H_{SP}^0 = 94\ km$	I	-	6.6	7.0	0	341	1%
$H_{SP}^0 = 100\ km$	III	-	6.4	7.2	0	341	2%
$H_{SP}^0 = 111\ km$	III	-	6.4	7.2	0	341	21%
$H_{SP}^0 = 122\ km$	IV	6.2	6.4	7.2	0	341	110%
$H_{SP}^0 = 141\ km$	IV	5.4	6.0	7.7	0	341	2800%
$H_{OP}^0 = 67\ km$	IV	5.4	6.0	7.7	0	341	2800%
$H_{OP}^0 = 70\ km$	IV	6.4	6.6	7.0	0	341	1300%
$H_{OP}^0 = 74\ km$	III	-	7.2	6.4	0	341	30%
$H_{OP}^0 = 77\ km$	II	-	7.6	6.1	0	341	4%
$H_{OP}^0 = 100\ km$	I	-	8.8	5.2	0	341	1%
$L_{OP}^0 = 500\ km$	IV	5.4	6.0	7.7	0	341	2800%
$L_{OP}^0 = 600\ km$	IV	5.4	6.0	7.7	0	384	690%
$L_{OP}^0 = 700\ km$	IV	5.6	6.0	7.7	130	371	630%
$L_{OP}^0 = 800\ km$	IV	5.8	6.0	7.7	231	364	14% [a]
$L_{OP}^0 = 1000\ km$	III	-	6.0	7.9	282	369	15%
$L_{OP}^0 = 1200\ km$	III	-	5.8	7.9	621	370	11%
$L_{OP}^0 = 1600\ km$	II	-	5.4	8.5	937	411	4%

[a] The total strain listed here is calculated along the middle vertical slice (5000 km away from side boundaries). For models $L_{OP}^0 \geq 800\ km$, the necking zones are away from this middle vertical slice. So, the total strain could be underestimated for these models. Considering that only model '$L_{OP}^0 = 800\ km$' achieved weakening level 'IV', the corrected total strain along its necking zone is ~600%. While the underestimation for other models is moderate and will not change the conclusion of this research.

As introduced in section 3.1.1, weakening levels 'I', 'II', 'III', 'IV' are determined by the minimum viscosity contour which is necked in the overriding plate during subduction. The higher the weakening level, the stronger the localised rheology modification observed within the overriding plate. All three groups of dual inward dipping subduction models manage to yield a variety of weakening levels in the overriding plate (Figure 10, a-c).

t_{rift} indicates the timestep when the overriding plate develops rifting extension (weakening level 'IV'), and a void value means that model fails to generate rifting extension within the overriding plate. It shows that only models achieving weakening level 'IV' develop rifting extension. t_{rift} increases with thicker or longer overriding plate, and decreases with thicker subducting plate.

t_{660} equals how much time the subducting plate (defined by its 1300 K isotherm) takes to sink to the depth of 660km. It is most sensitive to the variation of H_{OP}^{0}, while varying L_{OP}^{0} and H_{SP}^{0} generates less than ~1 Myr difference of t_{660} compared with a ~3 Myr difference when modifying H_{OP}^{0}. $\bar{v}_{sink}$ equals 460 km (the vertical distance from the initial slab tip depth to the depth of 660 km) divided by t_{660}. $\bar{v}_{sink}$ ranges from 5.2 to 8.5 cm/yr and the magnitude does not correlate with the weakening level or t_{rift}, i.e., high sinking rate does not necessarily lead to higher weakening level or faster rifting extension.

l_{n2n} is the horizontal distance between necking centres which may develop rifting extension during dual inward dipping subduction, i.e., secondary necking regions are excluded. The value of l_{n2n} is 0 km if there is only one necking centre within the overriding plate. l_{n2n} starts to increase with L_{OP}^{0} when L_{OP}^{0} is greater than ~700 km. l_{n2n} in Table 3 is recorded at the timestep of 4.4 Myr. It should be noted that, l_{n2n} may vary with time and the difference is at most ~250 km (Figure 4).

l_{n2t} marks the lateral distance from the centre of the necking area to its nearest trench at the 4.4 Myr timestep. For all simulations, l_{n2t} is in a narrow range of ~340-410 km and the variation is likely to originate from the fact that l_{n2t} is also time dependent. Since the average sinking rate is different for these models, different models may behave differently at the same timestep.

Total strain is calculated by integrating the average strain rate ($\overline{\dot{\varepsilon}_{II}}$ based on Equation (13)) with time throughout the 10 Myr simulation. All three groups of models generate a variety of total strain at the end of the simulation (Figure 10, d-f). For all models that develop rifting extension, the total strain is greater than 100%. Total strain in the range of 5% to 100% is observed from limited thinning up to significant extension. For models where the total strain is less than 5%, the weakening deformation is hardly observable in the overriding plate.

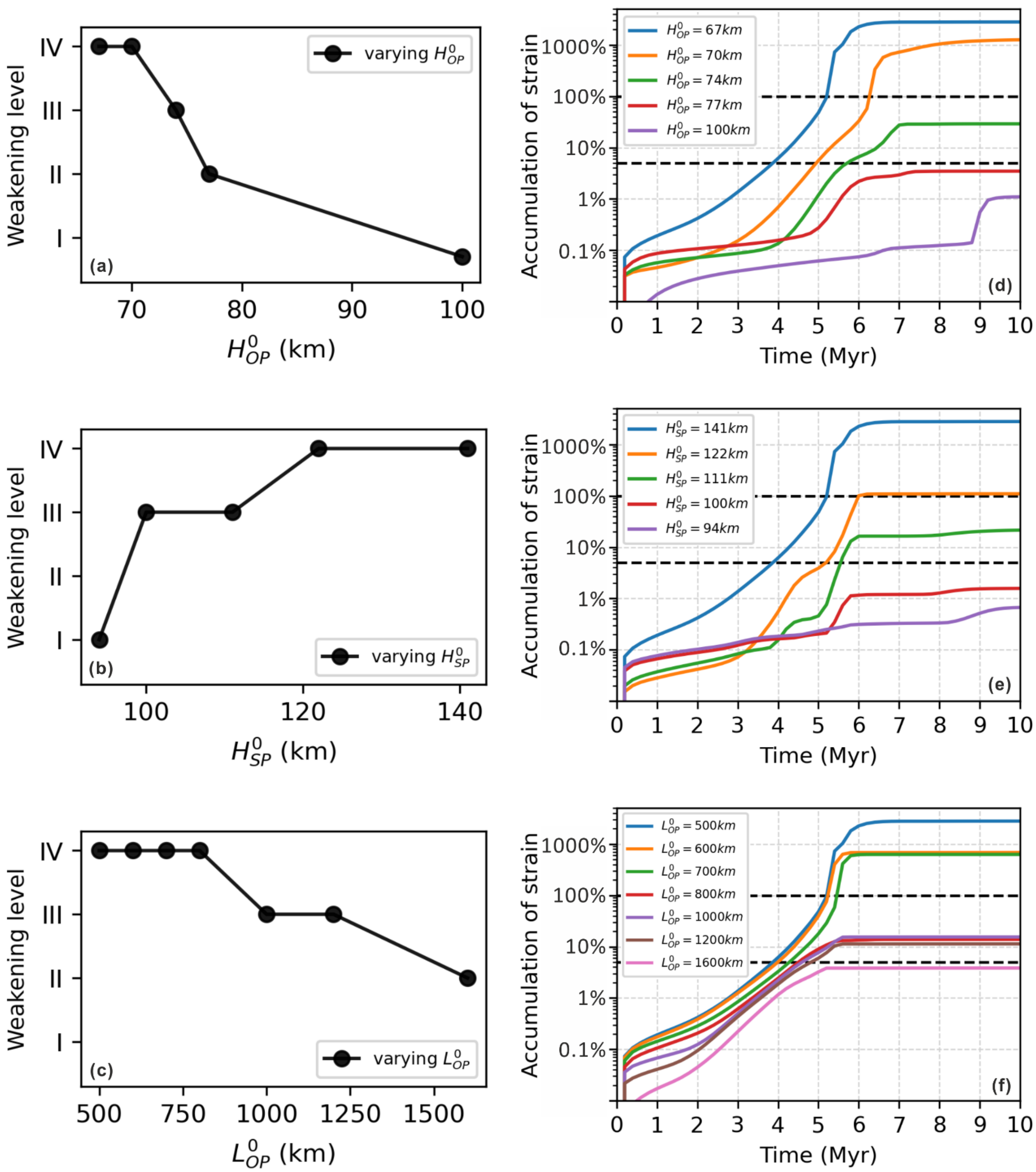

Figure 10. Key diagnostics used to characterise the rheology modification within the overriding plate. (a-c) Weakening level developed within the overriding plate. (d-f) Accumulation of strain in the middle of the overriding plate (5000 km away from the side boundaries).

By combing all the qualitative and quantitative diagnostics presented in these results, we classify three stretching states: 1) little or no lithosphere thinning and extension, discriminated by low weakening level up to level ‘II’, little total strain up to 5% and almost no thermal lithosphere thinning in the necking area; 2) limited lithosphere thinning and extension, identified by medium weakening level up to level ‘III’, medium total strain up to 30%, and limited thermal lithosphere thinning, e.g., ~15 km thinning for model ‘$H_{OP}^{0} = 74\,km$’ (Figure 7, c); 3) rifting and spreading extension, characterised by high weakening level up to level ‘IV’, high total strain over 100%, and total thinning of the thermal lithosphere during rifting extension.

4. Discussion

The results show that the non-steady state subduction provides a time window to develop progressive weakening within a uniform overriding plate. With appropriate conditions, tested in this research, e.g., thick enough H_{SP}^{0}, thin enough H_{OP}^{0}, short enough L_{OP}^{0}, different levels of stretching state, ranging from no thinning nor extension to rifting and spreading extension, can develop within the homogeneous overriding plate. The role that dual inward dipping subduction plays during the progressive weakening and the origin of the softening process are worth discussion.

4.1 The role dual inward dipping subduction plays

4.1.1 Creating fixed trailing boundary condition for the overriding plate

Due to the symmetric model setup, subducting plates on both sides are prone to advance or retreat simultaneously. This creates roughly equal and symmetric competing force from both ends of the middle plate during subduction. As a result, the mobility of the overriding plate is inhibited, and in comparing to single-sided subduction, it would be as if the velocity boundary condition on the overriding plate was fixed (Figure 11, a-c). This helps cultivating an ever-increasing stretching stress field and forming localised necking weak zones within the middle plate during non-steady state subduction. This is unlike the single sided subduction cases, where the mobile overriding plate can move as a whole to slow down the build up of deviatoric stress within the plate. Thus, the lack of mobility of the overriding plate plays a key role in the weakening process during subduction.

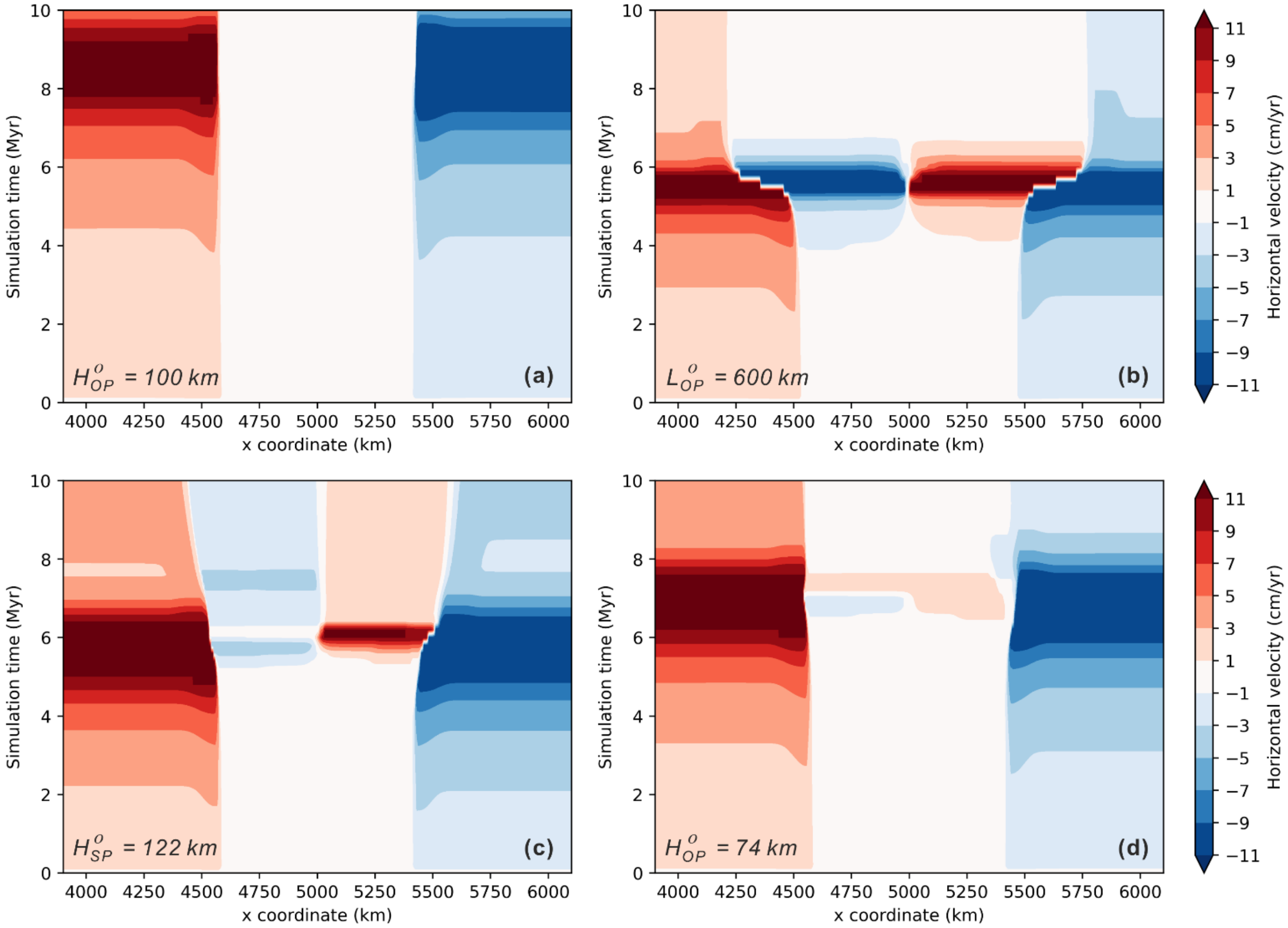

Figure 11. Temporal evolution of horizontal velocity along a lateral slice, x coordinate from 3900km to 6100 km, at the depth of 20 km from the surface. (a) model '$H_{OP}^{0} = 100\ km$', (b) model '$L_{OP}^{0} = 600\ km$', (c) model '$H_{SP}^{0} = 122\ km$', (d) model '$H_{OP}^{0} = 74\ km$'. The contour filling represents the variation of horizontal component of velocity vector throughout the 10 Myr simulation. Positive value means right-ward motion and negative value is left-ward motion. The white area represents that the plate is nearly stagnant. And the edge of the white area marks the interface between the subducting plate and overriding plate or rifting and spreading centre within the overriding plate.

The fixed boundary condition environment is likely to be favoured as long as on both sides the slab has symmetric trench motion tendencies. Once one side is prone to advance, or move slower than the other, then the fixed boundary condition effect is likely to weaken and the magnitude of the velocity of the overriding plate can increase from ~0 cm/yr to 1-3 cm/yr (Figure 11, d). But still, the overriding plate is not as mobile as a free mobile boundary condition in single subduction models, where the overriding plate can move as fast as 5 cm/yr as a whole during the non-steady state subduction (e.g., Chen et al., 2016).

In previous subduction models, a fixed boundary condition is achieved on the overriding plate by extending the overriding plate to the side boundary and applying a fixed velocity to the plate. It is suggested that such a boundary condition is responsible for the increased degree of deformation in the overriding plate compared with mobile plates (Chen et al., 2016; Erdős et al., 2021; Yang et al., 2019). A comparable effect is achieved by bringing in another subducting plate at the other end of the overriding plate. The fixed boundary condition effect is also observed in previous dual inward dipping subduction models (Dasgupta and Mandal, 2018; Holt et al., 2017; Lyu et al., 2019), but its role in affecting the weakening of the overriding plate was not addressed since the viscosity was only composition-dependent and did not change with evolving stress or temperature.

4.1.2 Stronger poloidal return flow

Our results show that varying the size of the overriding plate can affect the degree of extension within the overriding plate. Previous research shows that subduction can induce poloidal mantle return flow, which has been suggested to account for extensional deformation within the overriding plate, e.g., back-arc extension, supercontinent breakup (Chen et al., 2016; Dal Zilio et al., 2018; Erdős et al., 2021; Sleep and Toksöz, 1971). Previous research also implies that, a) increasing the thickness of the subducting plate (H_{SP}^{0}) can increase the net negative buoyancy thus leading to a stronger poloidal flow (Garel et al., 2014); b) lowering the thickness of the overriding plate (H_{OP}^{0}) can not only increase the net negative buoyancy by increasing the hanging slab area in the upper mantle, but also reduces the dissipation during subduction along the interface between two plates (Erdős et al., 2021). These two mechanisms also come into play for dual inward dipping subduction models.

In addition, dual inward dipping subduction models can yield a third way to strengthen the return flow. This is by combining the two separate poloidal convection flows, one from each subducting plate, as the length of the overriding plate (L_{OP}^{0}) shortens (Figure 3). This is shown for example by the velocity variation in both the horizontal (v_x) and vertical (v_y) direction at the depth of 75 km (Figure 12). For all dual inward dipping subduction models, the magnitude of v_x decreases gradually from ~2.5 cm/yr in the mantle wedge corner to 0 cm/yr underlying the middle part (~5000 km away from side boundaries) of the overriding plate (Figure 12, a). As L_{OP}^{0} changes, models with shorter overriding plate have greater v_x gradient along the lateral slice (Figure 12, b). The maximum magnitude of v_y increases from ~0.25 cm/yr to ~1.3 cm/yr, implying a faster upwelling flow, as the length of the overriding plate (L_{OP}^{0}) shortens (Figure 12, c-d). It is also noted that the necking area developed within the overriding plate (e.g., Figure 3) lies right above the maximum upwelling component of the return flow (Figure 12, c). The observation indicates a spatial correlation between the stronger poloidal return flow and the progressive weakening in the overriding plate.

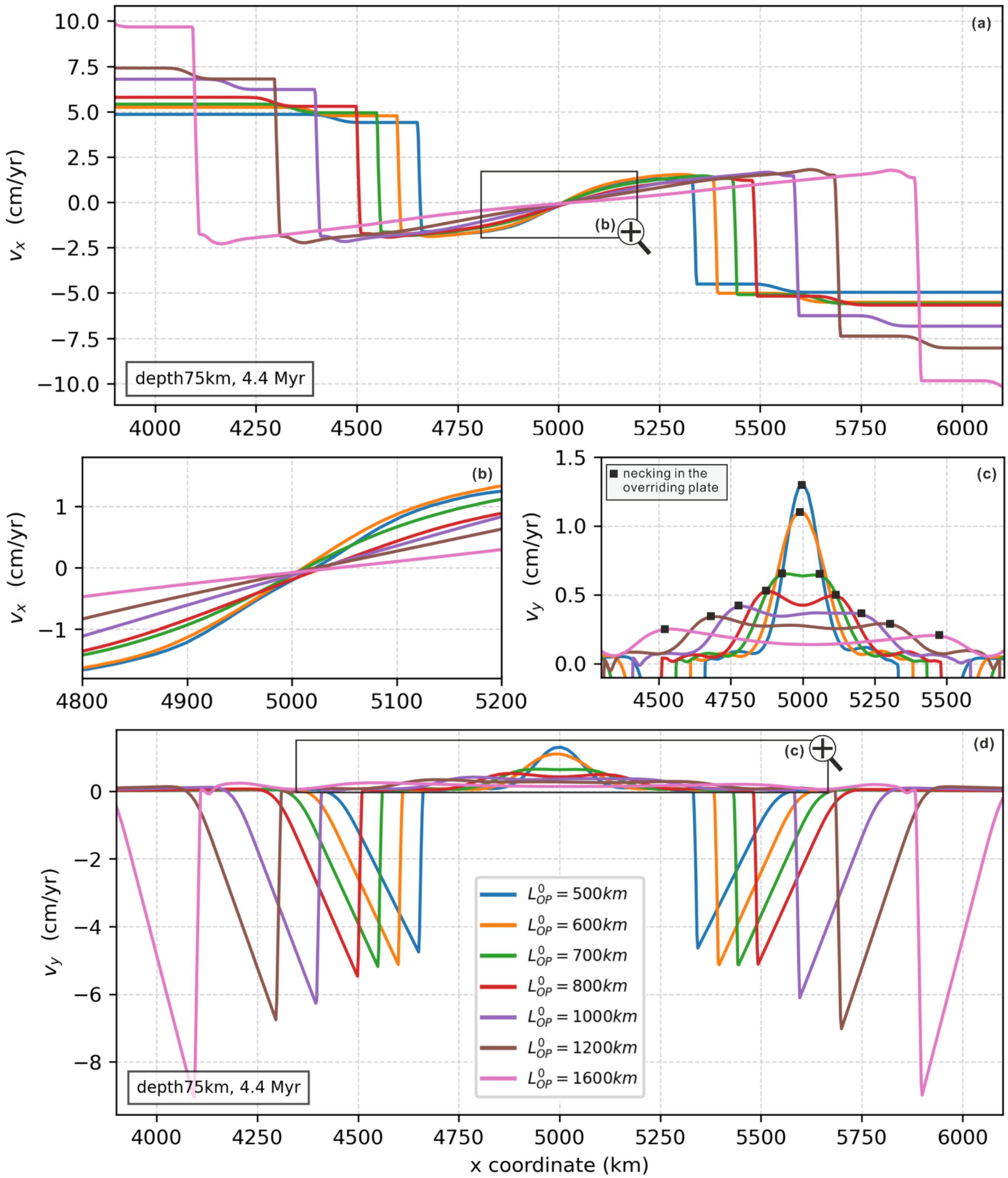

Figure 12. Velocity variation along a slice at the depth of 75 km, which is ~8 km below the 1300 K isotherm of the overriding plate, after 4.4 Myr simulation. (a, d) Horizontal and vertical component of velocity along the slice. (b) and (c) are zoom-in of (a) and (d) under the middle part of the overriding plate (5000 ± 200 km and 5000 ± 650 km away from the side boundaries respectively). Positive value means rightward or upward motion, and negative value represents leftward or downward motion. In (c), the horizontal coordinate of the necked region in the overriding plate is plotted as black square to visualize its spatial correlation with upwelling component of mantle wedge flow. All plots share the same legend listed in (d).

Previous research on subduction induced continental breakup implies that spreading extension develops above where the upwelling mantle flow diverges, flow which creates the highest shear stress gradient at the bottom of the overriding plate (Dal Zilio et al., 2018). This does not fully agree with our simulation results with varying L_{OP}^{0}. The divergent return flow is defined as the place where v_x changes direction. It always lies under the middle part (~5000 km away from the side boundaries) of the overriding plate for all models (Figure 12, a). However, the weakening area does not always develop in the middle of the overriding plate, e.g., when $L_{OP}^{0} \geq 800\ km$. Instead, it correlates better in space with the highest upwelling mantle flow velocity (Figure 12, c). The lateral distance from the highest upwelling component to the nearest trench is measured (Figure 12, d), and it is noted that the distance remains relatively constant at ~370 km for all models at 4.4 Myr. This suggests that the wavelength of the slab induced mantle wedge flow is not related with varying L_{OP}^{0}.

An interesting observation is that the subducting slab's sinking velocity increases (t_{660} decreases) with longer L_{OP}^{0} (Table 3), while the poloidal mantle flow gets weaker and the maximum weakening level in the overriding plate decreases. From the perspective of energy conservation, all the dynamic processes, e.g., plate motion, mantle convection, internal deformation etc., originates from the potential energy of the subducting slabs. This implies that more of the potential energy transfers into kinetic energy of the subducting plates instead of being consumed as dissipation energy in the overriding plates, as L_{OP}^{0} increases.

4.2 Overriding plate weakening mechanism

To understand the viscosity weakening mechanism in the necking area, the dependency of viscosity on the three variables, strain rate, temperature and pressure are examined. Averaged variables are calculated based on Equation (13) along the middle slice (~5000 km away from side boundaries) of the thermal lithosphere, where the necking weak zone develops. Each dependency investigation is divided into three subplots based on the regime of stretching state developed within the overriding plate. They are 1) little or no thinning and extension; 2) limited thinning and extension; 3) rifting and spreading extension.

4.2.1 Strain rate weakening

The scatter plot of viscosity dependency upon strain rate in the necking area (Figure 13, a-b) shows that when the magnitude of average viscosity ($\bar{\mu}$) is higher than $10^{21}\ Pa \cdot s$ (weakening level < 'IV'), $\bar{\mu}$ deceases linearly with increasing $\overline{\dot{\varepsilon}_{II}}$. For models which develop significant lithospheric thinning and extension within the overriding plate (Figure 13, c), i.e., weakening level 'IV' and $\bar{\mu} \leq 10^{21}\ Pa \cdot s$, $\bar{\mu}$ starts to decrease faster with increasing $\overline{\dot{\varepsilon}_{II}}$ than the former linear relationship. After the subducting slab reaches the lower mantle, $\bar{\mu}$ starts to increase linearly again with the decreasing $\overline{\dot{\varepsilon}_{II}}$, indicating a hardening process after the progressive weakening. For models which do not neck the iso-viscous contour of $10^{21}\ Pa \cdot s$ (e.g., $H_{OP} \geq 74\ km$), the path of hardening process is nearly reversely parallel to its initial weakening trace (Figure 13, a-b).

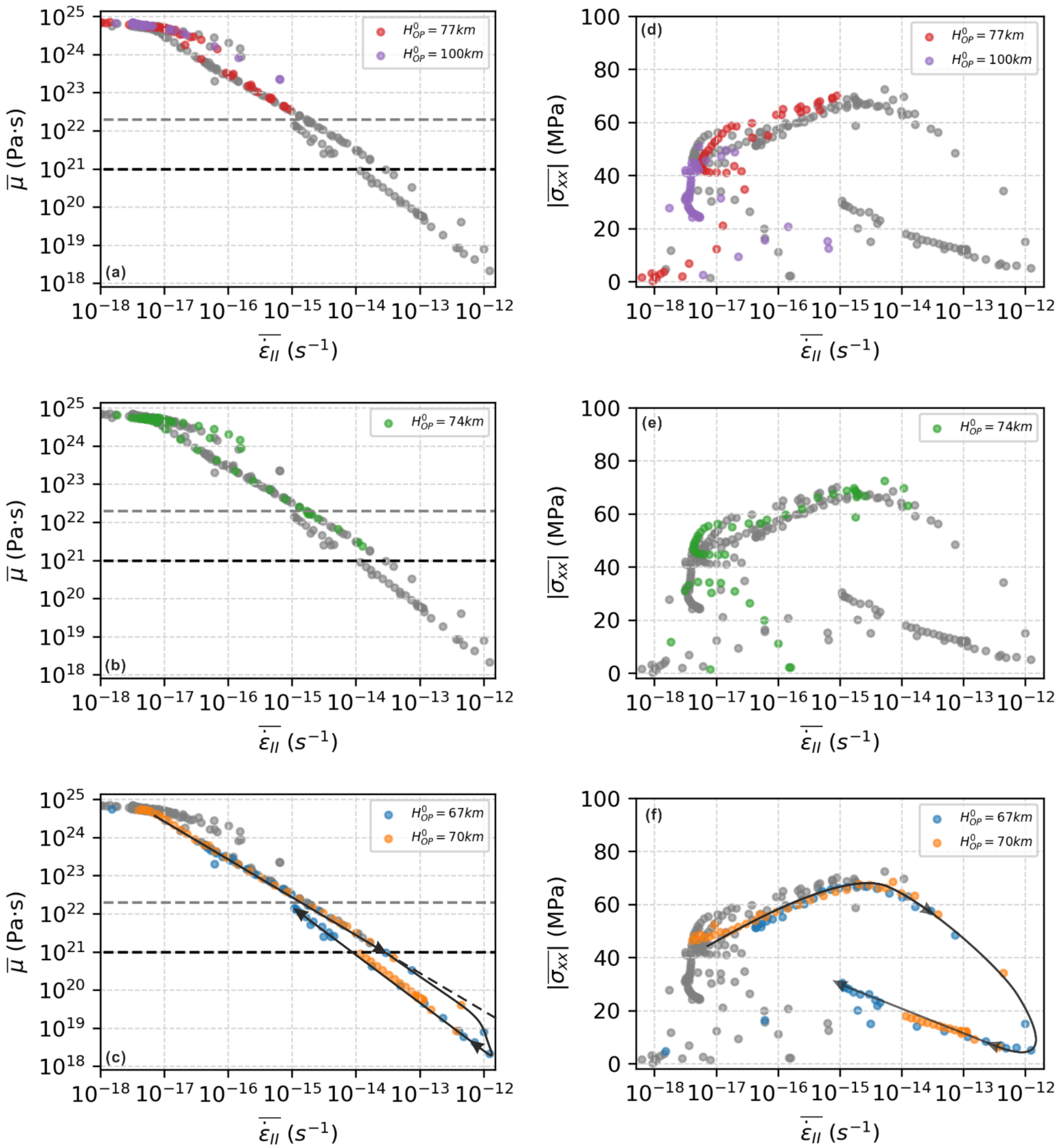

Figure 13. Scatter plot throughout the 10 Myr simulation of model series with varying thickness of the overriding plate. (a-c) $\bar{\mu}$ versus $\overline{\dot{\varepsilon}_{II}}$, (d-f) $|\overline{\sigma_{xx}}|$ versus $\overline{\dot{\varepsilon}_{II}}$. Variables in (a-f) are calculated based on Equation (13). The solid trajectory lines with arrow in (c) and (f) indicate the evolution orientation of the scatter points with time. Models in the same series of simulation but with different overriding plate stretching state are plotted in grey dots as comparison.

Then when $\overline{\dot{\varepsilon}_{II}}$ is lower than $\sim 10^{-14}\ s^{-1}$, the horizontal component of stress ($\overline{\sigma_{xx}}$) varies linearly with $\overline{\dot{\varepsilon}_{II}}$, indicating a highly viscous flow behavior within the overriding plate (Figure 13, d). But at larger strain rate (weakening level 'IV'), the viscosity decreases so rapidly with increasing strain rate that the stress, the very resistance to flow, decreases as well. The negative correlation between stress and strain rate suggests a decreasing plate strength which is proportional to $\bar{\mu} \times H_{OP}$ in the case of uniaxial stretching (Ribe, 2001). Such negative correlation has also been observed in a velocity-weakening rheology when strain rate exceeds a certain level (Bercovici et al., 2015), and in a crystal softening experiment (Poirier, 1985). The continuous plate strength reduction during dual inward dipping subduction also suggests that high strain rate may relate to the formation of new plate boundaries (Gueydan et al., 2014).

In this research, strain rate can affect the viscosity component related to yielding, Peierls and dislocation creep deformation (Equation (8), (9)). Thus, all three deformation mechanisms contribute to the softening process in the overriding plate. Considering that the sensitivity to strain rate decreases from yielding, to Peierls and dislocation creep respectively, their contribution to the viscosity drop may decrease accordingly. However, the evolution of the iso-viscous contour shows that the viscosity drop initiates from the surface (yielding) and the bottom of the plate (dislocation creep). Then the viscosity contour necks in the middle depth of the plate where Peierls creep dominates (Figure 2, b). This suggests that yielding and dislocation are more important for initiating plate softening than Peierls creep.

4.2.2 Thermal weakening and lithosphere thinning

The scatter plot of viscosity dependency upon the average temperature ($\bar{T}$) and pressure ($\bar{P}$) show that $\bar{T}$ and $\bar{P}$ have no correlation with viscosity drop when $\bar{\mu} \geq {\sim}2 \times 10^{22}\ Pa \cdot s$ (Figure 14, a, d). We note that $\bar{P}$ is a good indicator of lithosphere thickness. The thickness of thermal lithosphere starts to reduce as $\bar{\mu}$ keeps dropping to ~$10^{21}\ Pa \cdot s$. $\bar{T}$ still shows little correlation with $\bar{\mu}$, while

$\bar{P}$ becomes proportional to $\bar{\mu}$ (Figure 14, b, e). As $\bar{\mu}$ continues decreasing and rifting extension starts to develop, $\bar{T}$ shows a fluctuated and nonlinear correlation with $\bar{\mu}$, while $\bar{P}$ stays in a positive linear relationship (Figure 14, c, f).

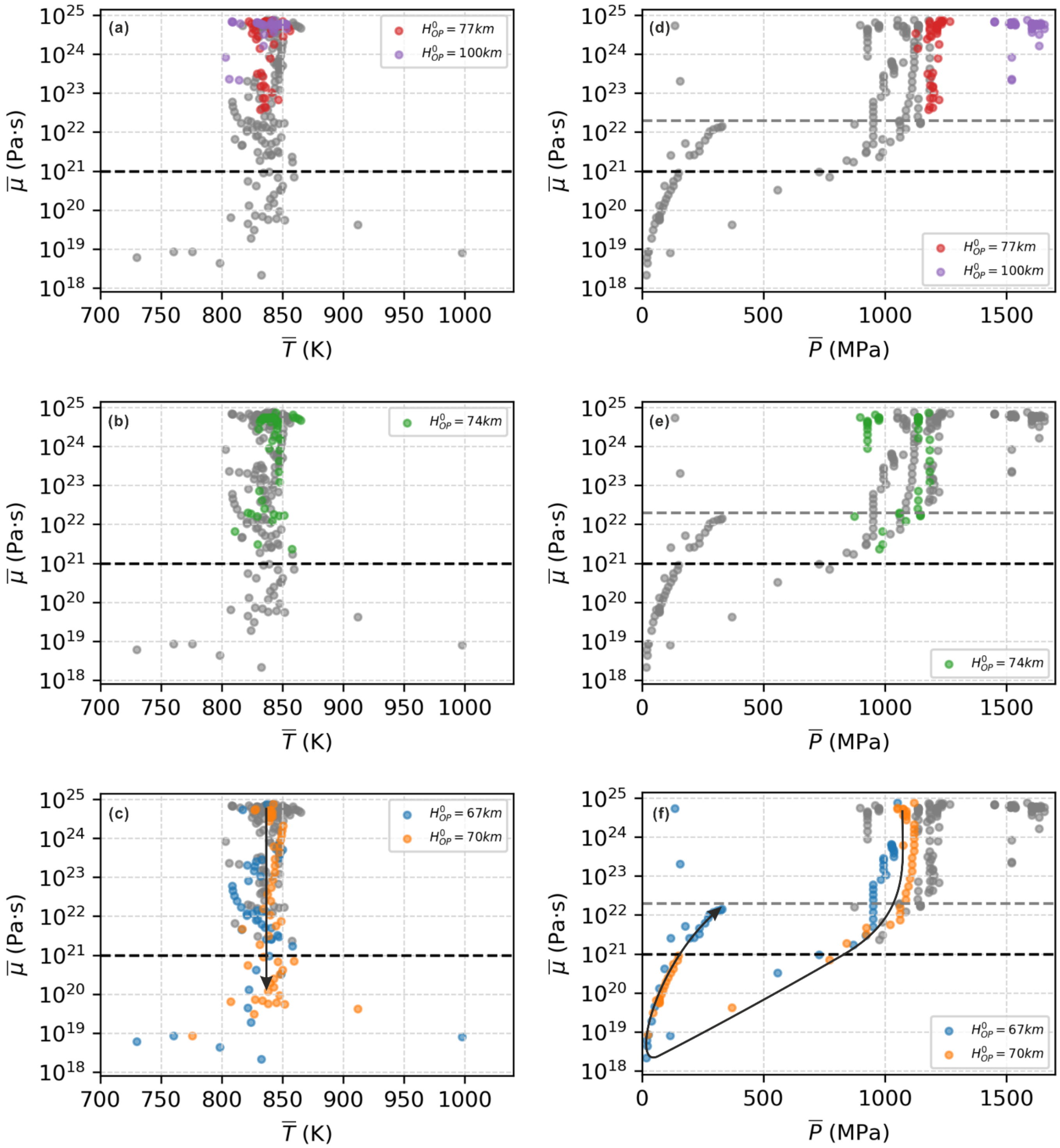

Figure 14. Scatter plot throughout the 10 Myr simulation of model series with varying thickness of the overriding plate. (a-c) $\bar{\mu}$ versus $\bar{T}$, (d-f) $\bar{\mu}$ versus $\bar{P}$ (mainly a measure of plate thickness). Variables in (a-f) are calculated based on Equation (13). Models in the same series of simulations but with different stretching states are plotted in grey dots for comparison.

Temperature increase, according to the rheology setup (Equation (8)), can lower the viscosity of Peierls, dislocation and diffusion creep. Temperature increase and lithosphere thinning can both contribute to weakening the overriding plate, but they may only play a role when the overriding plate is weakened to a certain level. For example, they may contribute to the additional viscosity drop seen in the non-linear relationship between $\overline{\dot{\varepsilon}_{II}}$ and $\bar{\mu}$ (Figure 13, c).

In general, three feedback weakening loops are recognised during the dual inward dipping subduction. Among them, the strain rate weakening mechanism plays a dominant role in lowering the viscosity of the overriding plate throughout the simulation, and it is a precondition to develop thermal weakening and lithosphere thinning, which strengthens the feedback weakening loop. The dominant role of strain rate weakening over thermal weakening is also reported in the interaction between upwelling plumes and overlying lithosphere (Burov and Guillou-Frottier, 2005). That is to say, the rheology and buoyancy parameters will be more important than the heat conduction parameters in producing different levels of rheology weakening within the overlying plate.

4.3 Limitations

The major contribution of this work is incorporating a composite rheology which depends on multiple parameters, e.g., temperature, pressure and strain rate. However, previous research indicates that viscosity can also be affected by hydrous fluids, partial melting, and grain size of minerals in subduction zones (Bercovici et al., 2015; Braun et al., 1999; England and Katz, 2010; Montési and Hirth, 2003). In particular, grain size reduction is likely to take place when strain builds up (Gueydan et al., 2014). Taking these parameters into consideration is likely to strengthen the feedback weakening process within the overriding plate during dual inward dipping subduction.

Subduction can generate convective mantle flow that includes both poloidal and toroidal components. The 2D models tested here neglect the effects of toroidal flow and the third dimension. This could amplify the magnitude of poloidal flow and its weakening effect applied within the overriding plate. Considering that poloidal component dominates over toroidal component during non-steady state subduction (Funiciello et al., 2004), and it is the poloidal cell that provides the relevant traction driving the deformation within the overriding plate (Király et al., 2017; Schellart and Moresi, 2013), the lack of toroidal flow would only have limited impact on the progressive weakening presented.

In this research, to obtain the designed wide range of plate thicknesses (67 km to 141 km), the half-space cooling model is used instead of the plate model. Plate thickness in plate model flattens when the plate age is greater than ~80 Ma, thus it is not ideal for investigating the effect of thick plates investigated here. We note that there is still great uncertainty in terms of how oceanic lithosphere thickness evolves with ocean floor’s age. Half-space cooling model was initially proposed to explain the age dependency of bathymetry and heat flow observed. However, this model does not fit these observations as well when the age of the oceanic plate is over 80 Ma. The plate model fits the flattening bathymetry and heat flow in older oceanic plates, but at the cost of applying an artificial temperature boundary condition at the bottom of lithosphere (Parsons and Sclater, 1977; Stein and Stein, 1992). Some question the existence of flattening seafloor bathymetry with age. There is research that indicates that excluding “anomalous oceanic crust”, such as sea mountains and hotspots, from the bathymetry dataset can reduce the flattening behaviour and make a half-space cooling model fit well with plates over 80 Ma (Korenaga et al., 2021; Korenaga and Korenaga, 2008). Another hypothesis suggests that half-space cooling model fits well with bathymetry along mantle flow lines instead of age trajectories in the Pacific (Adam and Vidal, 2010). The uncertainty regarding how oceanic lithosphere thickness evolves with ocean floor age, and the 2D nature of the models, requires the results of this study to be interpreted carefully before applying to Earth.

Bearing all the limits in mind, we cautiously compare our model predictions with observations in the North China Craton (NCC). Based on suture zone studies, the NCC may have experienced dual inward dipping subduction (Santosh, 2010; Windley et al., 2010). The Paleo-Asian Ocean subducts from the north of the craton, while to the southeast lies the subducting Pacific Plate. Surface wave tomography implies that the thickness of the overriding plate (H_{OP}^{0}), i.e., the NCC, decreases from ~150 km in the western block to ~70 km in the eastern block (Huang et al., 2009). The distance between the trenches of two subducting plates (L_{OP}^{0}) narrows beneath the eastern block. According to this work, we might suggest that the eastern block would suffer more weakening. This is consistent with the observation that rifting extension and magmatism intrusion, equivalent to weakening level 'IV', only develops in the eastern block, e.g., Bohai Bay Basin. So for now we only speculate that a dual subduction driven weakening process might have played a role in modifying the rheology and resulting in a variety of deformation patterns within the eastern block of the NCC, though to fully understand this would require further investigation utilising more advanced models, beyond the limits of this work.

4.4 Synoptic summary

The thermo-mechanical modelling here provides a generic understanding of the progressive weakening developed within a varying rheology overriding plate during dual inward dipping subduction. To summarize, dual inward dipping subduction holds a stronger tendency to weaken the overriding plate compared with single sided subduction. This is achieved by creating a fixed trailing boundary condition for the overriding plate and generating a stronger poloidal return flow underlying the overriding plate (Figure 15). The stronger poloidal mantle flow is exhibited as a higher horizontal velocity gradient and higher maximum magnitude of upwelling component underlying the overriding plate. It can also initiate higher degree of viscosity reduction, strain localisation and lithosphere thinning or even spreading extension within the overriding plate. Besides, a dual inward dipping subduction system with thinner and shorter overriding plate, and thicker subducting plate is likely to induce higher degree of viscosity reduction within the overriding plate (Figure 15, b-d).

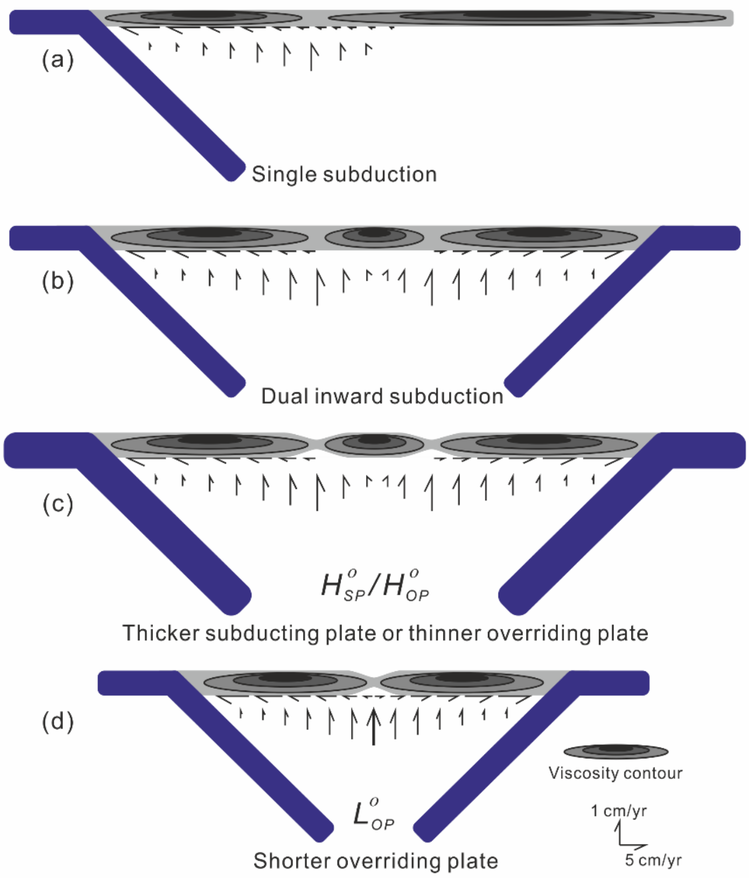

Figure 15. Synoptic comparison of different model setup's role in affecting the necking behaviour developed within the overriding plate. (a) Single sided subduction (e.g., Garel et al., 2014). (b) Dual inward dipping subduction. (c) Thickness of the subducting plate or overriding plate (H^0_{SP}, H^0_{OP}). (d) Length of the overriding plate (L^0_{OP}).

5. Conclusion

These 2-D thermo-mechanical numerical models demonstrate that dual inward dipping subduction can generate progressive weakening by lowering viscosity within the overriding plate on a ~10 Myr time scale. Three variables are investigated to understand what controls the maximum degree of weakening. It shows that the initial length (L_{OP}^{0}) and thickness (H_{OP}^{0}) of the overriding plate are negatively correlated with the maximum degree of weakening. While the initial thickness of the subducting plate (H_{SP}^{0}) positively relates to the maximum weakening level. The progressive weakening can result in a variety of irreversible stretching states ranging from 1) little or no lithosphere thinning and extension, to 2) limited thermal lithosphere thinning, and 3) localised rifting followed by spreading extension.

Comparing with single sided subduction, dual inward dipping subduction shows that it can reduce the magnitude of viscosity to a lower level within the overriding plate. Two aspects are analysed. On the one hand, a dual inward dipping subduction set-up effectively creates a dynamic fixed boundary condition for the middle (overriding) plate. This inhibits the mobility of the plate and helps promote localised strain deformation to accommodate the slab rollback tendency on both sides. On the other hand, when the initial length of the overriding plate is short enough ($L_{OP}^{0} \leq 800\ km$), dual inward dipping subduction can form a united upwelling mantle flow which interacts with the bottom of overriding plate and generates a stronger viscosity perturbation within it than single sided subduction models. As a result, dual inward dipping subduction can induce higher degrees of extension in the overriding plate compared with single sided subduction.

To understand the viscosity weakening mechanism in the necking area of the overriding plate, the dependency of viscosity on strain rate, temperature and pressure are evaluated separately. Three positive feedback weakening cycles are recognised, among which the strain rate weakening mechanism plays the dominant role in lowering the viscosity of the overriding plate throughout the simulation. Strain rate weakening is a precondition to initiate thermal weakening and lithosphere thinning, both of which only reinforce the feedback weakening loop during the rifting extension period.

Acknowledgement

We acknowledge the support of Advanced Research Computing at Cardiff (ARCCA) and the Supercomputing Wales project, which is part-funded by the European Regional Development Fund (ERDF) via the Welsh Government. Zhibin Lei also thanks the China Scholarship Council (CSC) for supporting the Ph.D. studentship and Cardiff University for an overseas fee waiver award.

References

Adam, C., Vidal, V., 2010. Mantle flow drives the subsidence of oceanic plates. Science (80-.). 328, 83–85. https://doi.org/10.1126/science.1185906

Bercovici, D., Tackley, P.J., Ricard, Y., 2015. The Generation of Plate Tectonics from Mantle Dynamics, in: Treatise on Geophysics: Second Edition. Elsevier B.V., Oxford, pp. 271–318. https://doi.org/10.1016/B978-0-444-53802-4.00135-4

Braun, J., Chéry, J., Poliakov, A., Mainprice, D., Vauchez, A., Tomassi, A., Daignières, M., 1999. A simple parameterization of strain localization in the ductile regime due to grain size reduction: A case study for olivine. J. Geophys. Res. Solid Earth 104, 25167–25181.

Bürgmann, R., Dresen, G., 2008. Rheology of the lower crust and upper mantle: Evidence from rock mechanics, geodesy, and field observations. Annu. Rev. Earth Planet. Sci. 36, 531–567. https://doi.org/10.1146/annurev.earth.36.031207.124326

Burov, E., Guillou-Frottier, L., 2005. The plume head-continental lithosphere interaction using a tectonically realistic formulation for the lithosphere. Geophys. J. Int. 161, 469–490. https://doi.org/10.1111/j.1365-246X.2005.02588.x

Burov, E.B., 2011. Rheology and strength of the lithosphere. Mar. Pet. Geol. 28, 1402–1443. https://doi.org/10.1016/j.marpetgeo.2011.05.008

Capitanio, F.A., Stegman, D.R., Moresi, L.N., Sharples, W., 2010. Upper plate controls on deep subduction, trench migrations and deformations at convergent margins. Tectonophysics 483, 80–92. https://doi.org/10.1016/j.tecto.2009.08.020

Chen, Z., Schellart, W.P., Strak, V., Duarte, J.C., 2016. Does subduction-induced mantle flow drive backarc extension? Earth Planet. Sci. Lett. 441, 200–210. https://doi.org/10.1016/j.epsl.2016.02.027

Chertova, M. V., Geenen, T., Van Den Berg, A., Spakman, W., 2012. Using open sidewalls for modelling self-consistent lithosphere subduction dynamics. Solid Earth 3, 313–326. https://doi.org/10.5194/se-3-313-2012

Dal Zilio, L., Faccenda, M., Capitanio, F., 2018. The role of deep subduction in supercontinent breakup. Tectonophysics 746, 312–324. https://doi.org/10.1016/j.tecto.2017.03.006

Dasgupta, R., Mandal, N., 2018. Surface topography of the overriding plates in bi-vergent subduction systems: A mechanical model. Tectonophysics 746, 280–295. https://doi.org/10.1016/j.tecto.2017.08.008

Davies, D.R., Wilson, C.R., Kramer, S.C., 2011. Fluidity: A fully unstructured anisotropic adaptive mesh computational modeling framework for geodynamics. Geochemistry, Geophys. Geosystems 12, n/a-n/a. https://doi.org/10.1029/2011GC003551

England, P.C., Katz, R.F., 2010. Melting above the anhydrous solidus controls the location of volcanic arcs. Nature 467, 700–703. https://doi.org/10.1038/nature09417

Erdős, Z., Huismans, R.S., Faccenna, C., Wolf, S.G., 2021. The role of subduction interface and upper plate strength on back-arc extension: Application to Mediterranean back-arc basins. Tectonics 40. https://doi.org/10.1029/2021tc006795

Faccenna, C., Becker, T.W., Holt, A.F., Brun, J.P., 2021. Mountain building, mantle convection, and supercontinents: Holmes (1931) revisited. Earth Planet. Sci. Lett. 564, 116905. https://doi.org/10.1016/j.epsl.2021.116905

Faccenna, C., Becker, T.W., Lallemand, S., Lagabrielle, Y., Funiciello, F., Piromallo, C., 2010. Subduction-triggered magmatic pulses: A new class of plumes? Earth Planet. Sci. Lett. 299, 54–68. https://doi.org/10.1016/j.epsl.2010.08.012

Fowler, C., 2005. The Solid Earth: An Introduction to Global Geophysics. Cambridge Univ. Press, Cambridge, U. K.

Funiciello, F., Faccenna, C., Giardini, D., 2004. Role of lateral mantle flow in the evolution of subduction systems: Insights from laboratory experiments. Geophys. J. Int. 157, 1393–1406. https://doi.org/10.1111/j.1365-246X.2004.02313.x

Garel, F., Goes, S., Davies, D.R., Davies, J.H., Kramer, S.C., Wilson, C.R., 2014. Interaction of subducted slabs with the mantle transition-zone: A regime diagram from 2-D thermo-mechanical models with a mobile trench and an overriding plate. Geochemistry, Geophys. Geosystems 15, 1739–1765. https://doi.org/10.1002/2014GC005257

Garel, F., Thoraval, C., 2021. Lithosphere as a constant-velocity plate: Chasing a dynamical LAB in a homogeneous mantle material. Phys. Earth Planet. Inter. 316, 106710. https://doi.org/10.1016/j.pepi.2021.106710

Gerya, T. V., Connolly, J.A.D., Yuen, D.A., 2008. Why is terrestrial subduction one-sided? Geology 36, 43–46. https://doi.org/10.1130/G24060A.1

Gueydan, F., Précigout, J., Montési, L.G.J., 2014. Strain weakening enables continental plate tectonics. Tectonophysics 631, 189–196. https://doi.org/10.1016/j.tecto.2014.02.005

Hall, R., Spakman, W., 2015. Mantle structure and tectonic history of SE Asia. Tectonophysics 658, 14–45. https://doi.org/10.1016/j.tecto.2015.07.003

Hirth, G., Kohlstedt, D., 2003. Rheology of the upper mantle and the mantle wedge: A view from the experimentalists, in: Eiler, J. (Ed.), Inside the Subduction Factory. American Geophysical Union, pp. 83–105. https://doi.org/10.1029/138GM06

Holt, A.F., Royden, L.H., Becker, T.W., 2017. The dynamics of double slab subduction. Geophys. J. Int. 209, 250–265. https://doi.org/10.1093/gji/ggw496

Huang, Z., Li, H., Zheng, Y., Peng, Y., 2009. The lithosphere of North China Craton from surface wave tomography. Earth Planet. Sci. Lett. 288, 164–173. https://doi.org/10.1016/j.epsl.2009.09.019

Huang, Z., Zhao, D., Wang, L., 2015. P wave tomography and anisotropy beneath Southeast Asia: Insight into mantle dynamics. J. Geophys. Res. Solid Earth 120, 5154–5174. https://doi.org/10.1002/2015JB012098

Karato, S. ichiro, 2010. Rheology of the Earth’s mantle: A historical review. Gondwana Res. 18, 17–45.

https://doi.org/10.1016/j.gr.2010.03.004

Király, Á., Capitanio, F.A., Funiciello, F., Faccenna, C., 2017. Subduction induced mantle flow: Length-scales and orientation of the toroidal cell. Earth Planet. Sci. Lett. 479, 284–297. https://doi.org/10.1016/j.epsl.2017.09.017

Király, Á., Funiciello, F., Capitanio, F.A., Faccenna, C., 2021. Dynamic interactions between subduction zones. Glob. Planet. Change 202, 103501. https://doi.org/10.1016/j.gloplacha.2021.103501

Korenaga, T., Korenaga, J., 2008. Subsidence of normal oceanic lithosphere, apparent thermal expansivity, and seafloor flattening. Earth Planet. Sci. Lett. 268, 41–51. https://doi.org/10.1016/j.epsl.2007.12.022

Korenaga, T., Korenaga, J., Kawakatsu, H., Yamano, M., 2021. A new reference model for the evolution of oceanic lithosphere in a cooling Earth. J. Geophys. Res. Solid Earth 126. https://doi.org/10.1029/2020JB021528

Kramer, S.C., Wilson, C.R., Davies, D.R., 2012. An implicit free surface algorithm for geodynamical simulations. Phys. Earth Planet. Inter. 194–195, 25–37. https://doi.org/10.1016/j.pepi.2012.01.001

Lynch, H.D., Morgan, P., 1987. The tensile strength of the lithosphere and the localization of extension. Geol. Soc. Spec. Publ. 28, 53–65. https://doi.org/10.1144/GSL.SP.1987.028.01.05

Lyu, T., Zhu, Z., Wu, B., 2019. Subducting slab morphology and mantle transition zone upwelling in double-slab subduction models with inward-dipping directions. Geophys. J. Int. 218, 2089–2105. https://doi.org/10.1093/gji/ggz268

Maruyama, S., Santosh, M., Zhao, D., 2007. Superplume, supercontinent, and post-perovskite: Mantle dynamics and anti-plate tectonics on the Core-Mantle Boundary. Gondwana Res. 11, 7–37. https://doi.org/10.1016/j.gr.2006.06.003

McKenzie, D.P., Roberts, J.M., Weiss, N.O., 1974. Convection in the earth’s mantle: towards a numerical simulation. J. Fluid Mech. 62, 465. https://doi.org/10.1017/S0022112074000784

Montési, L.G.J., Hirth, G., 2003. Grain size evolution and the rheology of ductile shear zones: From laboratory experiments to postseismic creep. Earth Planet. Sci. Lett. 211, 97–110. https://doi.org/10.1016/S0012-821X(03)00196-1

Parsons, B., Sclater, J.G., 1977. An analysis of the variation of ocean floor bathymetry and heat flow with age. J. Geophys. Res. 82, 803–827. https://doi.org/10.1029/JB082i005p00803

Perfit, M.R., Gust, D.A., Bence, A.E., Arculus, R.J., Taylor, S.R., 1980. Chemical characteristics of island-arc basalts: Implications for mantle sources. Chem. Geol. 30, 227–256. https://doi.org/10.1016/0009-2541(80)90107-2

Poirier, J.-P., 1985. Creep of crystals: High-temperature deformation processes in metals, ceramics and minerals (Cambridge Earth Science Series). Cambridge University Press, Cambridge. https://doi.org/10.1017/CBO9780511564451

Ribe, N.M., 2001. Bending and stretching of thin viscous sheets. J. Fluid Mech. 433, 135–160. https://doi.org/10.1017/S0022112000003360

Santosh, M., 2010. Assembling North China Craton within the Columbia supercontinent: The role of double-sided subduction. Precambrian Res. 178, 149–167. https://doi.org/10.1016/j.precamres.2010.02.003

Schellart, W.P., Moresi, L., 2013. A new driving mechanism for backarc extension and backarc shortening through slab sinking induced toroidal and poloidal mantle flow: Results from dynamic subduction models with an overriding plate. J. Geophys. Res. Solid Earth 118, 3221–3248. https://doi.org/10.1002/jgrb.50173

Sleep, N.H., Toksöz, M.N., 1971. Evolution of Marginal Basins. Nature 233, 548–550. https://doi.org/10.1038/233548a0

Stein, C.A., Stein, S., 1992. A model for the global variation in oceanic depth and heat flow with lithospheric age. Nature 359, 123–129. https://doi.org/10.1038/359123a0

Straub, S.M., Gómez-Tuena, A., Vannucchi, P., 2020. Subduction erosion and arc volcanism. Nat. Rev. Earth Environ. 1, 574–589. https://doi.org/10.1038/s43017-020-0095-1

Turcotte, D., Schubert, G., 2014. Geodynamics, 3rd ed. Cambridge University Press, Cambridge. https://doi.org/10.1017/CBO9780511843877

Uyeda, S., 1981. Subduction zones and back arc basins — A review. Geol. Rundschau 70, 552–569. https://doi.org/10.1007/BF01822135

Van Benthem, S., Govers, R., Spakman, W., Wortel, R., 2013. Tectonic evolution and mantle structure of the Caribbean. J. Geophys. Res. Solid Earth 118, 3019–3036. https://doi.org/10.1002/jgrb.50235

Wang, L., He, X., 2020. Seismic Anisotropy in the Java-Banda and Philippine Subduction Zones and its Implications for the Mantle Flow System Beneath the Sunda Plate. Geochemistry, Geophys. Geosystems 21, 1–19. https://doi.org/10.1029/2019GC008658

Windley, B.F., Maruyama, S., Xiao, W.J., 2010. Delamination/thinning of sub-continental lithospheric mantle under eastern China: The role of water and multiple subduction. Am. J. Sci. 310, 1250–1293. https://doi.org/10.2475/10.2010.03

Yang, T., Moresi, L., Gurnis, M., Liu, S., Sandiford, D., Williams, S., Capitanio, F.A., 2019. Contrasted East Asia and South America tectonics driven by deep mantle flow. Earth Planet. Sci. Lett. 517, 106–116. https://doi.org/10.1016/J.EPSL.2019.04.025